Università degli Studi di Padova

Dipartimento di Ingegneria Industriale DII
Corso di Laurea Magistrale in Ingegneria Aerospaziale

Satellite localization for gamma-ray pulsar observations in Low Earth Orbit

Relatore:
Prof. Stefano Debei
Corelatore:
Prof. Riccardo Rando

Laureando:
Riccardo Dal Moro
Matricola: 1197596

Anno accademico 2019/2020

Contents

List of Figures

Abstract (IT)

Contenuto della tesi

Gli obiettivi di questo lavoro di tesi sono la progettazione, lo sviluppo e la valutazione delle prestazione di un filtro di localizzazione satellitare basato su tecnologia GPS. Una possibile applicazione è a bordo di un CubeSat per dimostrazione scientifica di astrofisica a raggi gamma, in fase di studio persso l'Università degli Studi di Padova.

Per le fasi di sviluppo e test, la missione *Fermi* Gamma-Ray Space Telescope è stata presa come applicazione di riferimento. Mediante l'utilizzo dei dati delle telemetrie di *Fermi* abbiamo costruito il nostro filtro per poi confrontare i risultati con il filtro "NAV" sviluppato per *Fermi*.

Questo lavoro è stato diviso in due parti. La prima parte si è concentrata sul design e sullo sviluppo del filtro, è stato svolto uno studio di fattibilità analizzando una applicazione on-board ed una on-ground. Nel dettaglio è stato testato un metodo ai minimi quadrati non lineari ed un filtro di Kalman.
La seconda parte è stata la validazione del filtro di navigazione, applicando i risultati ottenuti ad uno studio scientifico che richiede una conoscenza della posizione del satellite molto precisa: il processo di timing di una pulsar millisecondo.

La sorgente che è stata scelta per la validazione è la pulsar millisecondo J1231-1411. Questa sorgente è molto debole per *Fermi* e non sarà possibile rilevarla mediante il piccolo dimostratore scientifico in studio per l'università. Sorgenti più luminose però presenterebbero un rateo osservato dal dimostratore comparabile con quello studiato, quindi questa validazione rappresenta un valido test.

Abastract (EN)

Content of the thesis

The purpose of this thesis work is the design, development and performance evaluation of a satellite's localization filter based on the GPS technology. One possible application is a proposed CubeSat demonstrator for MeV gamma-ray astrophysics being investigated at the University of Padova.

For the development and test the *Fermi* Gamma-Ray Space Telescope mission is taken as reference application. Using available real telemetry data from *Fermi*, we build our own navigation filter and compare its performance with the *Fermi*'s NAV filter.

The work is divided in two parts. The fist part is about the design and the implementation of the filter, with a feasibility study of an on-board and an on-ground version. In detail we tested a non linear least square approach and a Kalman filtering approach.
The second part is about the validation of the navigation filer with a real science application. We selected the most exacting analysis making use of the exact satellite position: the timing of a millisecond pulsar.

The source that we selected for the validation is the millisecond pulsar J1231-1411. This source is very faint for *Fermi* and it will never be seen by the small payload demonstrator of the CubeSat; on the other hand other bright pulsars would have a comparable statistics seen with the small demonstrator, so it is a reasonable test.

Chapter 1

Gamma-ray astrophysics from space

1.1 Gamma-ray direct observations

Gamma-ray astrophysics is the study of astrophysical phenomena in the energy range above a few 100s keV, as we can see from Figure 1.1 just above x-ray astrophysics. In this energy window many sources are available for investigation all across the Universe: local (e.g. the Sun), Galactic (e.g. pulsars) and remote (e.g. active galaxies).

In order to study directly this kind of events in an effective way we use orbiting satellite telescopes, to move above the atmosphere which is opaque to energetic photons[1].
Recent gamma-ray missions of interest are: CGRO (Compton Gamma Ray Observatory, NASA 1991), carrying 4 instruments to cover different energy ranges (BATSE and OSSE for lower energies, COMPTEL [0.75-30 MeV] and ERGET [20 - 30000 MeV] for higher energies), Fermi (Fermi Gamma-ray Space Telescope, NASA 2008) carrying the LAT and a lower energy Burst Monitor, and AGILE (Astrorilevatore Gamma ad Immagini Leggero, Italy, ASI, INAF, INFN, 2007).

In this thesis work we use data from *Fermi* LAT, a detailed description of this mission is given in Section 1.4

[1] An alternative is to perform indirect observations from the ground and look for the gamma rays being absorbed by the atmosphere

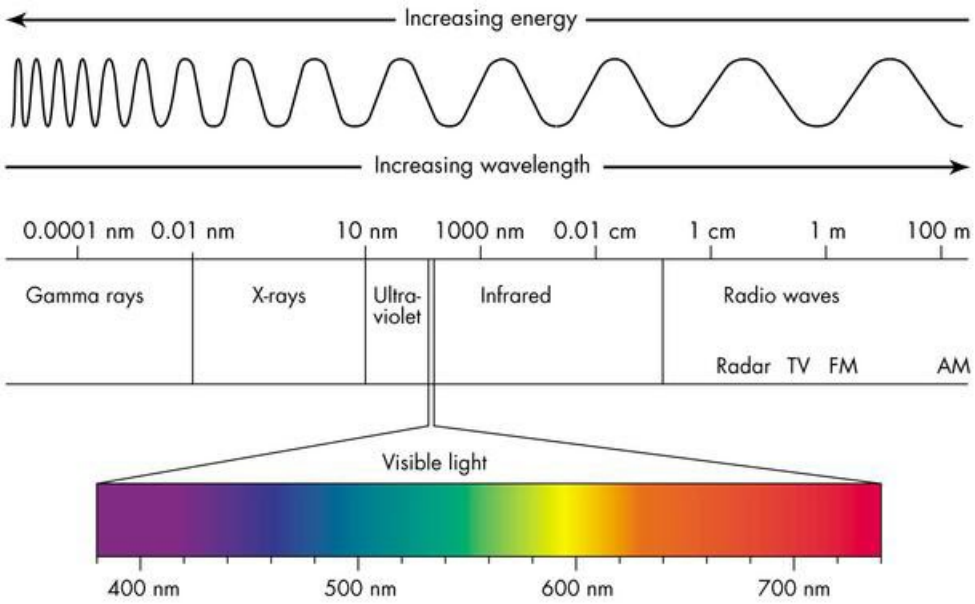

Figure 1.1: Electromagnetic spectrum description.

1.2 Future full scale MeV missions

Upcoming full scale missions (payload mass around 1 ton) are being proposed in the MeV energy range (bridging between the LAT range and x-ray instruments). Among these we mention:

- e-ASTROGRAM (enanched ASTROGRAM), an observatory space mission dedicated to the study of non-thermal Universe in the photon energy range from 0.3 MeV to 3 GeV [11]
- AMEGO (All-sky Medium Energy Gamma-ray Observatory), a probe class mission that combines high sensitivity in the 200 KeV - 10 GeV energy range with a wide field of view [21]

MeV mission of smaller scale are also being proposed. MEGA (Medium Energy Gamma-ray Astronomy) is a telescope concept aiming to improve sensitivity at medium gamma-ray energies (0.4 - 50 MeV) by at least an order of magnitude over

that of COMPTEL with a payload mass around 650 kg [8].

1.3 Nano scale MeV missions

Our team at the University of Padova is proposing a nano-satellite Compton telescope based on a silicon tracker and a Cesium-Iodide calorimeter [20] [23], as technological pathfinder for the coming MeV full-scale observatories but with a certain science potential on its own.

This Compton detector is currently in the design phase, managed as a series of thesis projects (bachelor and master) dealing with both engineering and scientific issues.

See [20],[7] (optimization of the tracker and calorimeter design), [22] (evaluation of the flux of cosmic protons along the orbit), [5] (study of the satellites material activation), [9] (sensitivity of the CubeSat to Gamma Ray Bursts).

1.4 *Fermi*-LAT

The *Fermi Gamma-ray Space Telescope* (FGST or *Fermi*) is a space observatory launched in 2008 by NASA and its mission is to observe the Universe in gamma rays from a Low Earth Orbit (LEO). *Fermi* orbit is a circular LEO with an altitude of 550 km and an inclination of 25.8 deg.

The main instrument on board *Fermi* is the Large Area Telescope (LAT), this is an imaging, wide field-of-view telescope that cover an energy range from ~ 20 MeV to > 1 TeV [6].

The performance of the scientific payload is described in `https://www.slac.stanford.edu/exp/glast/groups/canda/lat_Performance.htm` and references therein. Here we mention only a few relevant figures. As mentioned above the energy range covers from a few 10's MeV to a couple of TeV. The angular resolution depends on the photon's energy, it goes from about 10° at 100 MeV down to about 0.1° above 10 GeV; selecting data around a source we have to favor the lower energy end. The efficiency is usually given in terms of the effective area, i.e. the scaling factor between source flux (in ph/cm^2/s) and instrument count rate (in counts/s).

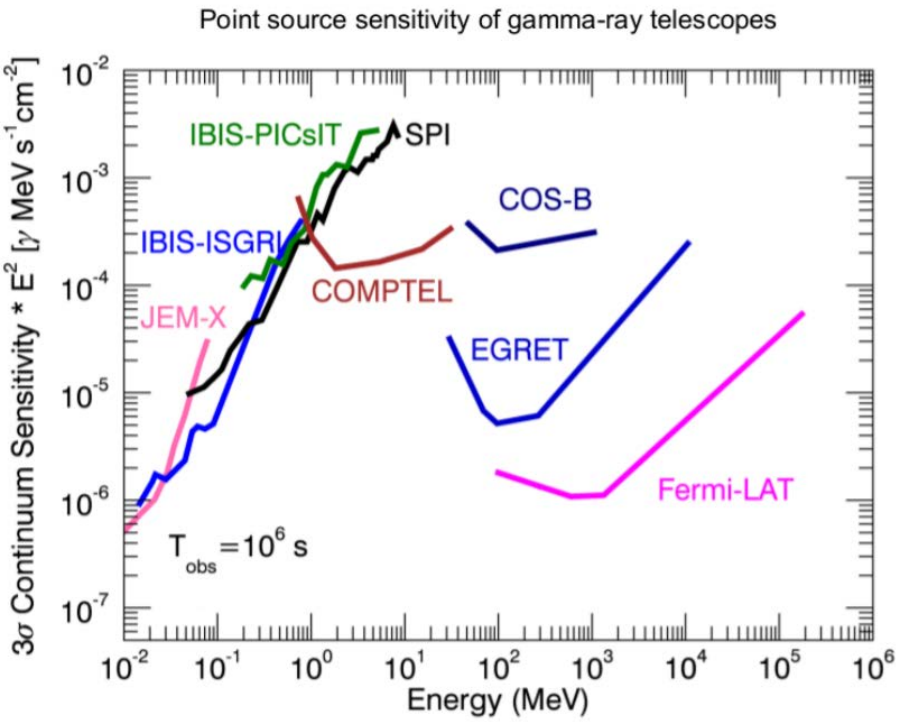

Figure 1.2: *Fermi-LAT* continuum sensitivity (the faintest observable flux as a function of energy for a point source with continuum spectrum) compared to other space telescopes.

It reaches up to $\sim$ 0.7 to 1 m^2 around 1 GeV for normal incidence, depending on the event selection, and almost constant up to a few 100's GeV where it drops; this is relevant because pulsar spectra decrease rapidly with energy in this range, so the lower the low energy cut the fewer events we keep, but as we have seen the lower we go the larger the selection radius and the higher the background we collect. Background for point sources includes the bright diffuse emission from the Galactic medium, especially relevant for Galactic sources such as pulsars. Depending on the source location and the LAT pointing history an additional background source is the very bright Earth limb, where gamma rays are being produced by cosmic proton hitting the atmosphere. During normal operation the LAT axis faces away from the Earth but it swings towards the orbit poles periodically, and at times the limb gets into the edges of the field of view.

Fermi mounts a General Dynamics Viceroy-4 GPS receiver (see Appendix). Each

detected photon is timestamped using the internal clock time. This is based on the PPS signal from the GPS driving a 10-MHz oven controlled oscillator and in turn a 20-MHz stabilized scaler giving the fraction of a second. The residuals in the scaler time when a PPS arrives are used to keep track of e.g. drift. The specifications allow for a ± 0.6 μs drift per minute under loss of GPS.
Localization in orbit is obtained on board from the GPS raw location processed by a Kalman filter, giving usually residuals < 20 m.

Chapter 2

Pulsars and timing

2.1 Pulsars

Pulsars are neutron stars (NS) characterized by fast rotation and high magnetization.
These bodies are extremely dense: the mass is comparable to the mass of the Sun but the radius is of the order of few tens of kilometers. They produce an energetic beam from the magnetic poles, converting rotational energy into electromagnetic radiation at all wavelengths. If the magnetic poles are not aligned with the rotation axis the pulsar behaves like a "lighthouse", causing electromagnetic pulses every time the beam crosses the observer's line of sight. In Figure 2.1 is reported a schematic representation of a rotating NS.

The first pulsar was detected in 1967 as a series of periodic radio pulses. In the 1970's pulsars were observed in gamma rays, but the identified sources were only the brightest: Crab and Vela. In the 1990's CGRO discovered some new gamma-ray pulsars but the game changer was *Fermi-LAT*: as of today it detected more than a hundred pulsars, including dozens of radio-quiet gamma-ray pulsars and millisecond pulsars [3] [10].

The timing of a millisecond pulsar is probably the scientific analysis, in gamma astrophysics, placing most exacting requirements on the satellite's positional and clock uncertainties. In particular a millisecond pulsar can have a pulse amplitude of ~ 0.1 ms or less: to reconstruct this we have to locate the satellite with an accuracy of a few km at worst.

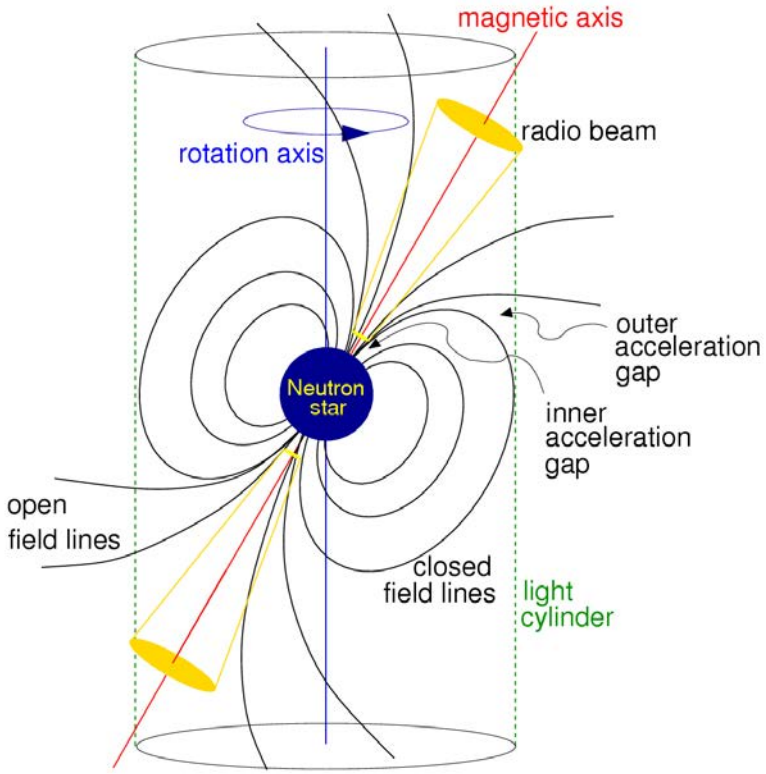

Figure 2.1: Schematic representation of a rotating NS (not in scale) [19].

2.2 Timing

Pulsar timing is performed by tracking Time of Arrival (ToA) of the photons and reconstructing of the pulse profile, assigning to each detected photon the rotational phase of the pulsar at the time of its emission. A phase histogram typically shows one or two emission peaks, corresponding to the emission regions crossing the line of sight. In Figure 2.2 is reported a basic observational setup required for pulsar timing [19].

In the gamma range the brightest pulsar is Crab, with a flux of 10^{-5} ph/cm^2/s above 100 MeV, with an effective area of ~ 1 m^2 (*Fermi*-LAT under optimal conditions) we can detect approximately 1 photon every 10 seconds, and the faintest

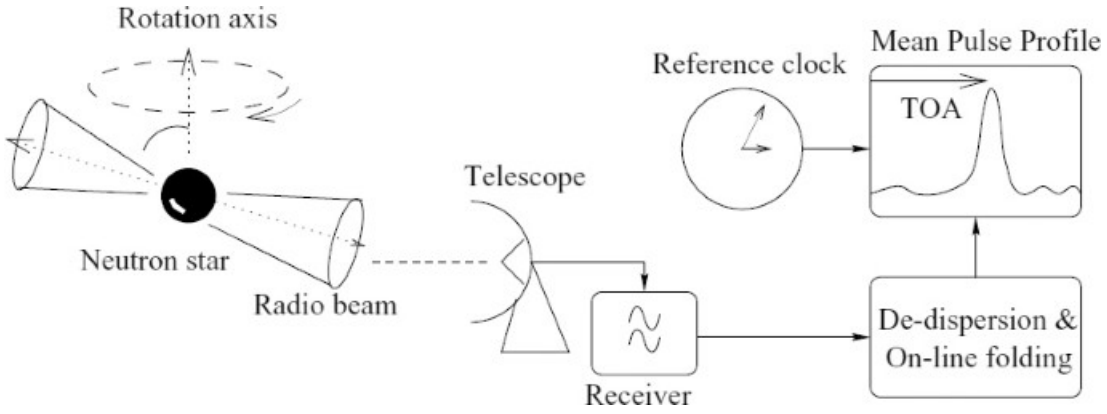

Figure 2.2: Basic concept of a pulsar timing observation [19].

pulsars detected have fluxes smaller by more than three orders of magnitude. Since the rotational periods are from ~ 1 ms to ~ 0.4 s the data is sparse and the folding process is needed. This process consists in phase-stacking many pulses to get an averaged pulse profile with high signal-to-noise ratio (S/N or SNR).

In the gamma study of a pulsar, each ToA is measured directly from the timestamp of the event. From these ToAs we build the phase histogram combining the ToAs with the pulsar ephemeris.
In Figure 2.3 the phase histogram of the Crab pulsar seen by LAT is reported. The pulsar period of rotation is about 33 ms, so the pulse width of 0.05 phase units correspond to ~ 1.5 ms.
This implies that we need a time resolution of the signal better than 0.5 ms to avoid smearing the peaks. Correspondingly, in case of a millisecond pulsar the resolution needed for the timing process is of the order of 10's μs.

In gamma rays we timestamp each photon and get the ToA in the topocentric reference frame (i.e. centered on the telescope position). We need to relate the ToA to the Solar-system barycentric (SSB) frame that with good approximation is an inertial frame (co-moving with the pulsar). Another advantage of the change in the reference frame is that the computed data can easily combined with ToAs measured in different locations at different times.

After the transformation to the barycentric system we have to describe the rotational motion of the pulsar. In the SSB the rotational period of a pulsar is nearly constant over the time of the observations: in the *Fermi*-LAT catalog period derivatives are around 10^{-14} s/s for normal pulsars and 10^{-20} s/s for millisecond pulsars.

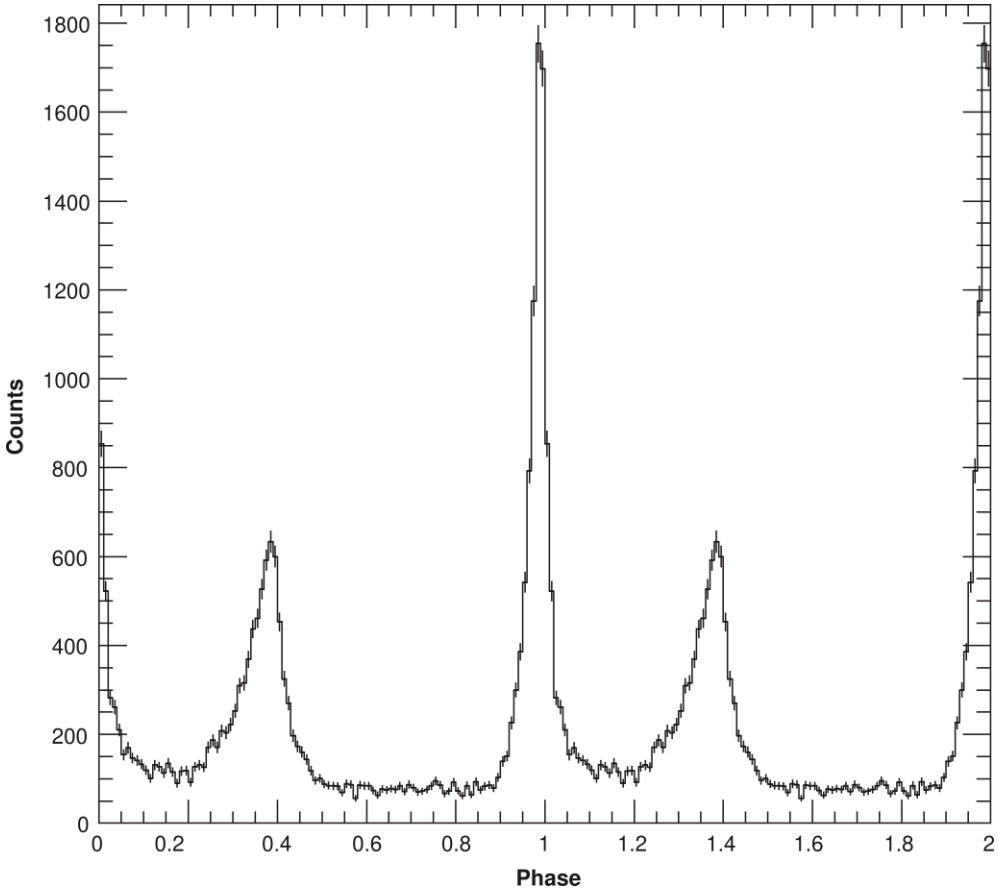

Figure 2.3: Phase histogram for the Crab pulsar in gamma rays, from [2]. Mind that 2 full phases are shown to avoid clipping the main peak.

Therefore we can express the time dependent phase as a Taylor expansion:

$$N(t) = N_0 + \dot{\nu}_0(t - t_0) + \frac{1}{2}\ddot{\nu}_0(t - t_0)^2 + ... \tag{2.1}$$

Where N_0 and t_0 are arbitrary reference phase and epoch ν_0 is the rotational frequency and $\dot{\nu}_0$, $\ddot{\nu}_0$ are its first and second derivative at the reference epoch.
Is important to notice that the observed rotational phase at each ToA is defined modulus an integer number of rotations. The average propagation time from source to detector, excluding the motion of the satellite in the SSB frame and any proper motion of the source, is absorbed into the arbitrary phase offset.

Observed ToAs can be compared to the predicted ToAs, and the differences are called "timing residuals". The uncertainties on the reconstruction of the pulsar's phase are: intrinsic (e.g. instabilities of the pulsar's rotation), on the inferred rotational parameters, and instrumental. The latter includes timing and location errors; see also Section 2.4.

Errors in deriving the rotational parameters lead to characteristic residual distributions. In Figure 2.4 are reported four different pulsar timing examples:

- Panel (a) reports a good solution with a residual random distribution with a zero mean
- Panel (b) shows the effect of an error in the frequency derivative
- Panel (c) shows an error in the position (sinusoidal trend with one year period)
- Panel (d) shows the error due to an un-modeled proper motion of the pulsar

2.3 Ephemeris

The rotation of each pulsar is characterized by its ephemeris. This is usually provided as a set of parameters describing the timing model as we discussed previously. The main information reported in the ephemeris are given in Table 2.1, where we follow the naming convention used by the TEMPO2 software, see Section 2.5.

The parameters in the ephemeris depend on time and are given at a set reference time (the epoch), and are valid in the specified time intervals. From the *Fermi GRST* is possible to get an open source table of published ephemeris for timing LAT Pulsars [13].

2.4 Pulsars with *Fermi*-LAT

of the scientific outputs of the *Fermi* mission is the pulsar catalog [3] which contains pulsars with a period ranging from ~ 400 to ~ 1 ms. The integrated measured fluxes at energy > 100 MeV goes from 10^{-5} ph/cm^2/s for the brightest down to a factor 10^4 less for the faintest. Given an effective area of ~ 1 m^2 under optimal conditions, this means that our data are sparse (1 photon every many periods).

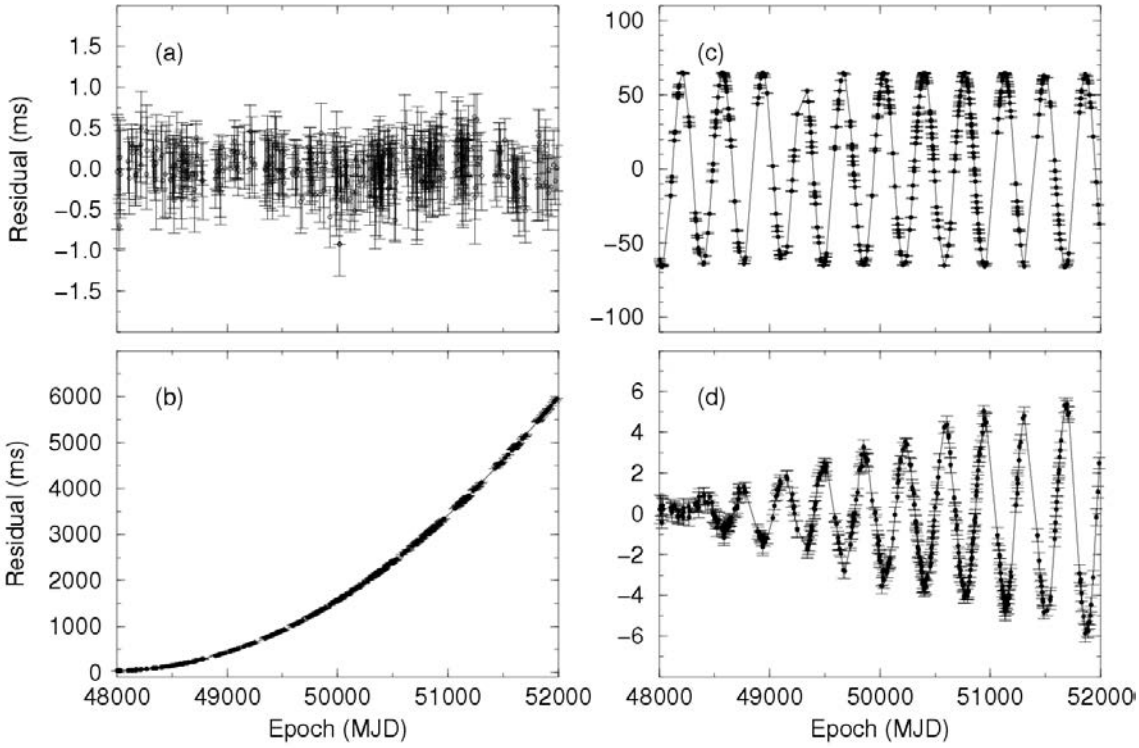

Figure 2.4: Residuals due to error on the fitting parameters [19].

In Figure 2.5 the periods and the periods derivative of known pulsars of the catalog are shown. As we can see, standard pulsars and millisecond pulsars are located in specific areas of this plot, a consequence of the different nature of these sources.

For the validation of the filter we performed a timing analysis of a millisecond pulsar. We selected J1231-1411 (T$\sim$ 3.6 ms). We used the ephemeris in preparation for the *Fermi* LAT catalog (a slightly updated version of the publicly available ones, developed for the third version of the catalog).
Other tools from *Fermi* used in the validation phase of the filter are the data about the events from the open source archive. In Section 2.5 the TEMPO2 software is described, briefly we use this software to compute the phase histogram. This plug-in reports the phase histogram, some statistic indicators and the computed phase of each photon.

LAT-related uncertainties on pulsar timing come mainly from 2 sources: the timing uncertainties on the event timestamp, based on the internal clock, and uncertainties on the telescope location in space. In this work we focus on the latter and

Parameter	Units	Description
PSRJ	String	Pulsar Name
RAJ	sex-hr	Right Ascension (J2000)
DECJ	sex-deg	Declination (J2000)
PEPOCH	MJD	Period Epoch (Modified Julian Date)
F0	Hz	Fundamental freq of the PSR
F1	Hz/s	First derivative of rotational freq
F2	Hz/s/s	Second derivative of rotational freq
POSEPOCH	MJD	Position Epoch
DM	pc/cm3	Dispersion Measure
START	MJD	Time the eph is valid from
FINISH	MJD	Time the eph is valid till
BINARY	String	The binary model used (if any)
EPHVER	Integer	The eph version

Table 2.1: Ephemeris parameters as found in a TEMPO2 ephemeris file for TEMPO2 see Section 2.5.

consider the former to be negligible.

2.5 Timing with TEMPO2

TEMPO2 is a software package for the analysis of pulsar pulse ToA [12] and it is an updated version of the TEMPO software.

A *Fermi* plug-in for TEMPO2 is available [14] that allows to compute a pulsar rotational phase for for each photon in a *Fermi LAT* event file. As described in Section 2.2 the first operation done by the plug-in is the computation of the telescope position in function of time in order to convert it in the barycentric reference system. After this operation for each photon the software calculates the time it was emitted by the pulsar, the rotational phase of the latter using the ephemeris file, computes an histogram of the pulse profile and the significance of the observation of a pulsed signal [17]

The software requires three file to work in its minimal setup.

- The `ft1` file is the photon file in `fits` format. It lists the selected events, giving

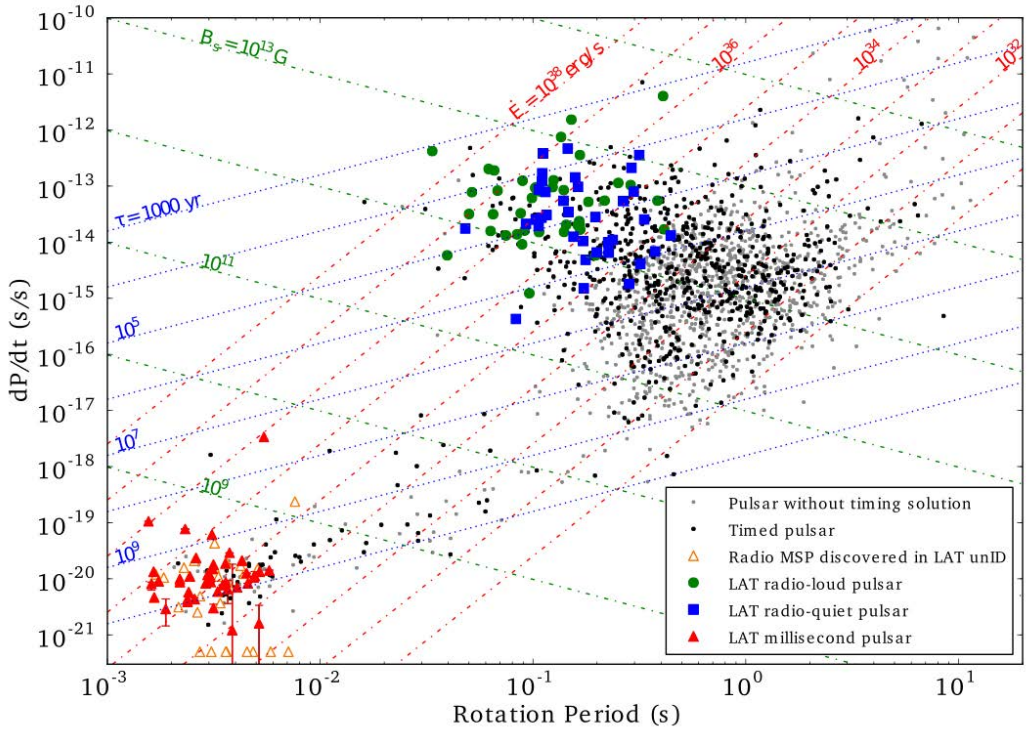

Figure 2.5: Periods and period derivatives of known pulsars, from [3]. Gamma-ray pulsars in the *Fermi*-LAT catalog are indicated in color.

the time of detection, arrival direction, energy, etc.

- The `ft2` file is the spacecraft position file in `.fits` format. It lists the location of the telescope and its attitude as a function of time, typically at intervals of 30 s.

- The `parfile` contains the pulsar ephemeris.

Chapter 3

Satellite localization

3.1 Orbital motion

The motion of two bodies due to their mutual gravitational attraction is known as two body problem, if the mass of the main body is $m_1 >> m_2$ the motion of the smaller body refers to the restricted two body problem. The ideal Keplerian dynamic model is:

$$\ddot{\mathbf{r}}(t) = \frac{\mu}{r^3}\mathbf{r}(t) \tag{3.1}$$

Where $\ddot{\mathbf{r}}(t)$ is the acceleration vector, $\mathbf{r}(t)$ represent the orbital radius components and μ is the Earth's standard gravitational parameter.

In the real case this model is affected by perturbations. Figure 3.1 is reports the intensity of the perturbations related to the orbit highness, main perturbations in LEO are:

- Gravitational perturbations
- Atmospheric drag

3.1.1 Gravitational perturbations

The main perturbation that affects a LEO satellite orbit is given by the effect of the non uniformity of the Earth gravitational field.

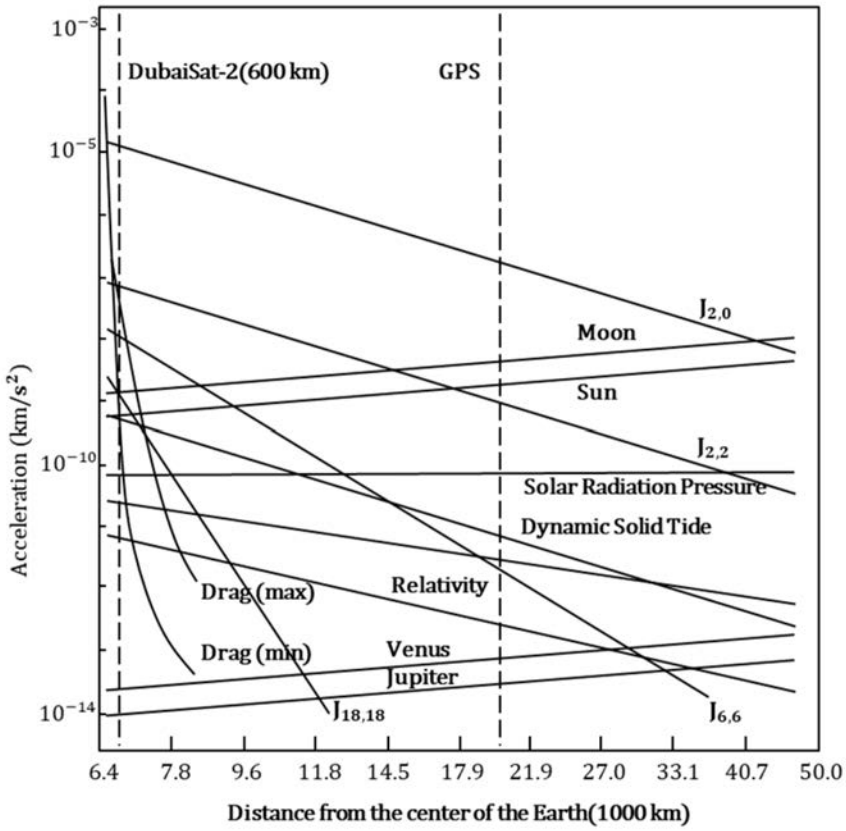

Figure 3.1: Intensity of the perturbations related to the orbit highness, from [18].

A simplified model is obtained considering only the first few zonal harmonics. If we consider only the J_2 effect the equation of motion from Equation 3.1 become:

$$\begin{aligned}
\ddot{x} &= -\frac{\mu x}{r^3}\left[1 + J_2\left(\frac{R_e}{r}\right)^2 \frac{3}{2}\left(1 - 5\frac{z^2}{r^2}\right)\right] \\
\ddot{y} &= -\frac{\mu y}{r^3}\left[1 + J_2\left(\frac{R_e}{r}\right)^2 \frac{3}{2}\left(1 - 5\frac{z^2}{r^2}\right)\right] \\
\ddot{z} &= -\frac{\mu z}{r^3}\left[1 + J_2\left(\frac{R_e}{r}\right)^2 \frac{3}{2}\left(3 - 5\frac{z^2}{r^2}\right)\right]
\end{aligned} \tag{3.2}$$

If we add the J_3 and J_4 effects to the Equation 3.2, we obtain the model described

in Equation 3.3:

$$
\begin{aligned}
\ddot{x} &= -\frac{\mu x}{r^3}\Big[1 + J_2\Big(\frac{R_e}{r}\Big)^2\frac{3}{2}\Big(1 - 5\frac{z^2}{r^2}\Big) + J_3\Big(\frac{R_e}{r}\Big)^3\frac{5}{2}\Big(3 - 7\frac{z^2}{r^2}\Big)\frac{z}{r} + \\
&\quad - J_4\Big(\frac{R_e}{r}\Big)^4\frac{5}{8}\Big(3 - 42\frac{z^2}{r^2} + 63\frac{z^4}{r^4}\Big)\Big] \\
\ddot{y} &= -\frac{\mu y}{r^3}\Big[1 + J_2\Big(\frac{R_e}{r}\Big)^2\frac{3}{2}\Big(1 - 5\frac{z^2}{r^2}\Big) + J_3\Big(\frac{R_e}{r}\Big)^3\frac{5}{2}\Big(3 - 7\frac{z^2}{r^2}\Big)\frac{z}{r} + \\
&\quad - J_4\Big(\frac{R_e}{r}\Big)^4\frac{5}{8}\Big(3 - 42\frac{z^2}{r^2} + 63\frac{z^4}{r^4}\Big)\Big] \\
\ddot{z} &= -\frac{\mu z}{r^3}\Big[1 + J_2\Big(\frac{R_e}{r}\Big)^2\frac{3}{2}\Big(3 - 5\frac{z^2}{r^2}\Big) + J_3\Big(\frac{R_e}{r}\Big)^3\frac{5}{2}\Big(6 - 7\frac{z^2}{r^2}\Big)\frac{z}{r}\Big] + \\
&\quad + \frac{\mu}{r^2}J_3\Big(\frac{R_e}{r}\Big)^3\frac{3}{2} + \frac{\mu z}{r^3}J_4\Big(\frac{R_e}{r}\Big)^4\frac{5}{8}\Big(15 - 70\frac{z^2}{r^2} + 63\frac{z^4}{r^4}\Big)
\end{aligned}
\tag{3.3}
$$

3.1.2 Atmospheric drag

After the gravitational perturbations the atmospheric drag is the main perturbation that affects a LEO satellite, the effect of this perturbation is the dissipation of the satellite energy. Drag phenomena changes orbital elements (mainly the semi-major axis and the eccentricity).

The acceleration due to the aerodynamic drag involves different physical proprieties of satellite and atmosphere. This means that a good knowledge of each parameter is required to determining the drag effects.
In Equation 3.4 is reported the basic equation of the aerodynamic drag:

$$
\mathbf{a}_{drag} = -\frac{1}{2}\frac{c_D A}{m}\rho v_{rel}^2\frac{\mathbf{v}_{rel}}{|\mathbf{v}_{rel}|} \tag{3.4}
$$

The term $(c_D A)/m$, also known as ballistic coefficient (BC), is related to satellite's proprieties. In detail:

- c_D is the satellite's coefficient of drag
- A is the exposed cross-sectional area (defined as the area normal to the satellite's velocity)
- m is the satellite mass

Another satellite-related parameter is the relative velocity $\mathbf{v}_{rel}$. This is not the velocity represented on the state vector but is the satellite velocity relative to the atmosphere, it depends from satellite's velocity and position.

The atmospheric density (ρ) is the most difficult parameter to determine. The density of the upper atmosphere is influenced by several factors as solar activity, local time (day-night time), latitude and longitude and many more. For detailed descriptions see [27].

3.1.3 Other perturbations

Gravitational and drag perturbation are the main disturbing forces on a LEO satellite. Other perturbations that could affect the motion of a satellite are:

- Third-Body accelerations: massive body as Moon and Sun affect the satellites on higher altitude orbits.
- Solar radiation pressure: as the atmospheric drag, it is a non conservative perturbation and it becomes more important at higher altitudes. This perturbation is related to the pressure that the solar radiation flux has on the satellite. The magnitude of this force depends on the cross-sectional area exposed to the flux, the intensity of the flux and shadowing effects on the spacecraft.

3.1.4 Orbit propagation

For orbit propagation we used a 4th order Runge-Kutta (RK4) method. This method is a single-step that combine the state at one time with the rates at several other times, based on the state value at time t_0.

The RK4 is often preferred for this kind of applications because it doesn't require state values before the t_0 to start the integrator. The Runge-Kutta methods evaluate the function of motion at intermediate points and these value are used only one time for the integration. To deepen this topic and for other integration methods see [27].

3.2 Reference systems

3.2.1 Earth-Centered Inertial

The Earth-Centered Inertial (ECI) is a Cartesian reference frame that has the origin located at the Earth's center. The x-axis is fixed in a direction relative to the celestial sphere (this definition of the x-axis give the inertial characteristic of the frame because the axis does not rotate with the Earth). The z-axis is normal to x and coincides with the Earth's rotation axis, it passes through the north pole. The y-axis completes the frame.

In Figure 3.2 is described the J2000 ECI reference frame. This is a common ECI frame, the x-axis is aligned with the mean equinox of the current epoch (in this case the mean equinox at 12:00 terrestrial time on 01/01/2000). The x-y plane lies on the Earth's equatorial plane.

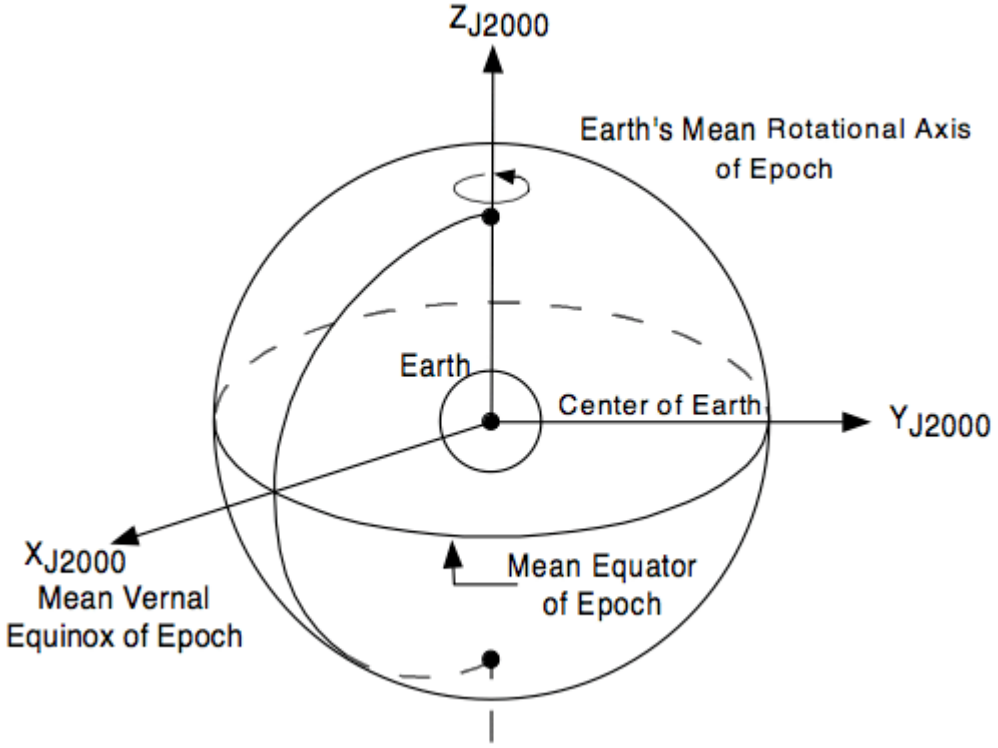

Figure 3.2: ECI-J2000 reference system representation [24].

3.2.2 Earth-Centered, Earth-Fixed

The Earth-Centered, Earth-Fixed (ECEF) is a Cartesian reference frame and like the ECI frame the origin is placed at the Earth's center. The x-axis points to the intercept of the mean Greenwich meridian and the equator, the z-axis coincides with the Earth's rotation axis and the y-axis completes the frame.

Due to the definition of the x-axis the ECEF frame rotates with the Earth. This frame is commonly the best choice to represent Earth related objects that need a location with respect to the Earth's surface.

3.3 Orbit determination and estimation

Orbit determination is one of the first problem that astronomers tried to solve. In the early 1800s Gauss and Legendre worked independently to estimate and predict the orbit of the asteroid Ceres, the result was a technique close to the least-squares method that will be discussed in the next session.

In the modern epoch the main application of the orbit determination passed from the estimation of orbits of bodies around the Sun to the space surveillance and the study of bodies in orbit around the Earth.
Determination of satellite position and orbit estimation has an important role due to the increasing population of spacecrafts in LEO. There are two different kinds of approach to get the state vector (position and velocity) of an orbiting body: ground based and space based techniques.

3.3.1 Ground based techniques

This kind of approach is based on measurements provided by ground stations that use radars or laser beams to track the targets.

Radar Ranging

The satellite radar ranging (SRR) was one of the first orbital positioning system, it is based on:

- measurement of the aiming angle (relative to the station's coordinates).
- measurement of the satellite/radar range, obtained from the delay of the echo.
- measurement of the range rate, obtained from the Doppler shift.

The SRR can be implemented with a network of radar stations that give a precise measurement using the trilateration process. This trilateration ranging technique allow to know the state of the satellite with a (1σ) position error < 6 m and a (1σ) velocity error < 1 cm/s [15]. The main advantage of SRR is the capability to detect bodies without on board receiver or dedicated laser reflectors.

Laser Ranging

The Satellite Laser Ranging (SLR) is the most accurate ranging technique with a position accuracy error < 1 cm (is important to remember that the accuracy of the

ranging process is correlated with the length and the resolution of the laser pulses). The distance measurement is derived from the time of flight of a laser pulse that travels from the station to the satellite; target spacecrafts have to be equipped with dedicated retro-reflectors. Figure 3.3 shows a representation of the SLR system architecture.

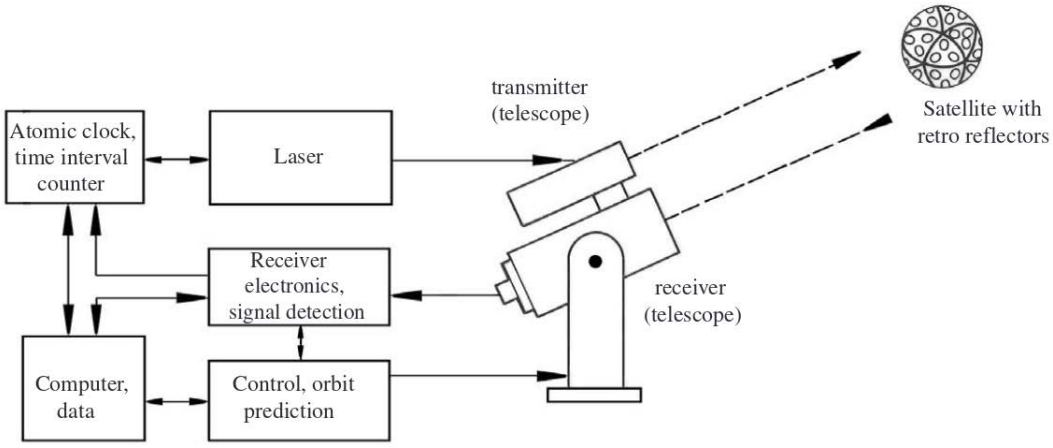

Figure 3.3: Principle of SLR, from [25].

The ground based techniques provide data characterized by a very good accuracy, despite the high accuracy potential the main disadvantages are:

- High costs related to the building and the management of the ground stations.
- Dependence on weather conditions.
- Non homogeneous tracking data distribution due to the fact that the target will be in the station's field of view for a limited time interval.

3.3.2 Space based techniques

A space based orbit determination system uses instrumentation on board the satellite to get the state vector. Due to its accuracy and due to the low cost of a receiver the GPS-based orbit determination is the most common choice and is widely used for real-time precise positioning in LEO.

3.4 Global Navigation Satellite System

The Global Navigation Satellite System (GNSS) is a system of satellite constellations used to provide position and velocity of a receiver, giving an high precision timing of the events. These processes are known as Position Navigation and Timing (PNT) and are guaranteed at any time in every point of the Earth's surface (and sky) independently of weather conditions. The only the only constraint is the visibility of a minimum number of satellites from the receiver position.

Currently the main GNSS constellations are the US Global Positioning System NAVigation Satellite Timing And Ranging (shortly GPS NAVSTAR), the Russian GLObal NAvigation Space System (GLONASS) and the European Galileo. Other systems are the Chinese BeiDou, the Japanese QZSS1 and the Indian NAVIC/IRSNSS.

The GNSS positioning is based on the trilateration process. This technique is similar to the triangulation but uses range measurements instead of angle measurements. In the GNSS case is uses a passive ranging (one way) based on the time of flight of the signal from the satellites to the receiver. Because ranging is a measurement of distance, a measurement of distance using the time of flight is called pseudoranging.

Let us consider the GPS NAVSTAR as an example of GNSS.

The GPS NAVSTAR program started in 1973 for military purposes and was extended to civil activities in 1991. The first satellite was launched in 1978 and the constellation was completed in 1994.
The Global Positioning System is composed by three different segments: the Space segment (SS), the Control segment (CS) and the User segment (US).

3.4.1 Space Segment

The SS is composed by 24 satellites that are orbiting in six orbital planes. For each orbital plane there are four satellites with an interval of 60 degrees of longitude. The orbits are circular at 20200 km of altitude with an inclination of 55 degree, each satellite has an orbit period of an half sidereal day with the same ground track each day. A representation of the constellation is in Figure 3.4.

As we will see later, the minimum number of satellites needed for the positioning

process is four; with the actual expanded constellation there are usually more than four satellites in sight from any point of the Earth's surface. This redundancy of satellites in sight ensures a good positioning process at any time in every place.

Figure 3.4: Representation of GPS NAVSTAR representation constellation.

3.4.2 Control Segment

The CS is a network of facilities located along the equatorial line that tracks, monitors and commands each satellite of the system. This network is composed of:

- A Master Control Station and an Alternate Master Control Station
- 11 command and control antennas
- 16 monitoring sites

In Figure 3.5 are shown the locations of the facilities in a map provided by the Official U.S. government information about the Global Positioning System (GPS) and related topics

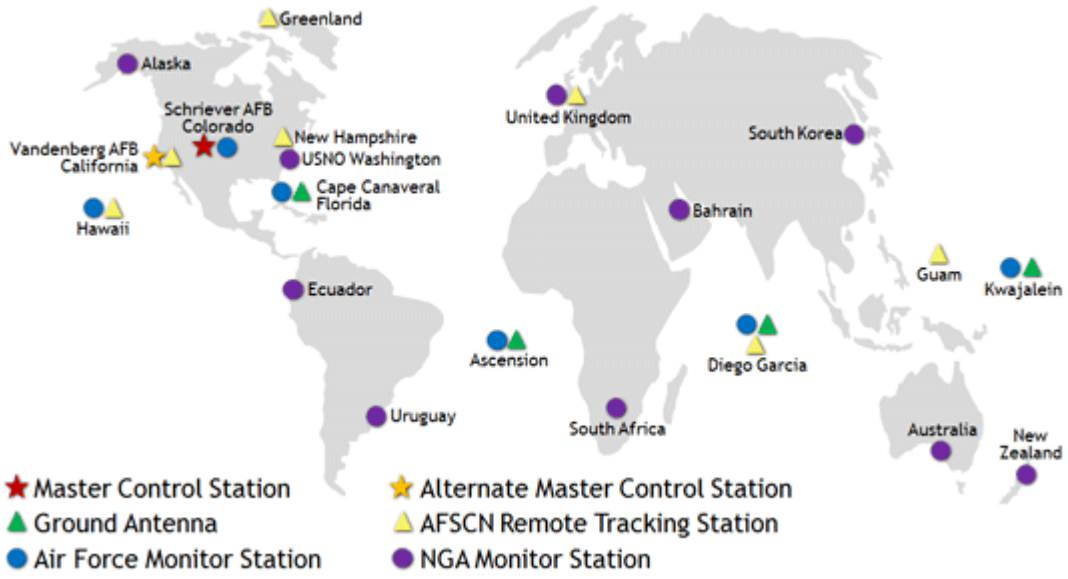

Figure 3.5: Map of the GPS NAVSTAR CS facilities.

The Monitor Stations check operational status, position and velocity of the satellites. Also the orbital errors and the clock drift of each satellite are monitored in order to keep it into the operational range of precision.
The data provided by the Monitor Stations are sent to the Master Control Station that computes position and velocity of all the constellation. These computed information is sent to the GPS satellites with a navigational update in order to synchronize the atomic clocks and correct the ephemeris of the satellites in their internal orbital model.

3.4.3 User Segment

The User segment is composed by every user of the GPS system. They could use the system for PNT in different situation as maritime, aerial and terrestrial navigation. A receiver decodes the signals from the satellites and computes its position.

3.4.4 GPS Signal

The GPS works on two frequencies based on $f_0 = 10.23$ MHz provided by the internal atomic oscillator :

- L1 signal = $f_0 \cdot 154 = 1575.42$ MHz
- L2 signal = $f_0 \cdot 120 = 1227.60$ MHz

For the L1 signal a CDMA (Code Division Multiple Access) technique is used: a low-bitrate navigation message (50 Hz) is encoded with an high-bitrate pseudorandom (PRN) code that is different for each satellite (the receiver needs to know the PRN codes to reconstruct the message).
This signal is also known as Coarse Acquisition Code (C/A) and is characterized by a data transmission at 1023 chips per millisecond. The positioning process based on the C/A code is called SPS (Standard Positioning System) and is for civilian uses.

The L2 signal is encoded with a different pseudorandom code called Precision Code (P-code) with a repeat period of one week. The P-code has a data transmission of 10.23 million chips per second (corresponding a frequency of 10.23 MHz) and is used for military purposes, it can be encrypted with an additional code. In this case is called P(Y) code and the message is reconstruct only by equipment with the decryption key. The positioning system based on the P-code is called PPS (Precise Positioning System).

In Figure 3.6 is shown the modulation scheme for L1 and L2.

In addition to the PNR code, position and time of each GPS satellite needs to be known from the receiver, this information are encoded in the navigation message.
This navigation message contains:

- The GPS date and time and the status of the transmitting GPS satellite
- The ephemeris of the transmitting GPS satellite (4 hours of validity)
- The almanac, containing status and orbital information of every satellite of the constellation

3.4.5 Timing

In order to keep the time synchronization error low, the GPS uses the satellites clocks instead of the receiver clock for the timing process. The receiver clock is usually a low cost quartz clock that has an accuracy worse than one part in a million, that is not enough precise (an error of 1 millisecond means a 300 meters error for the

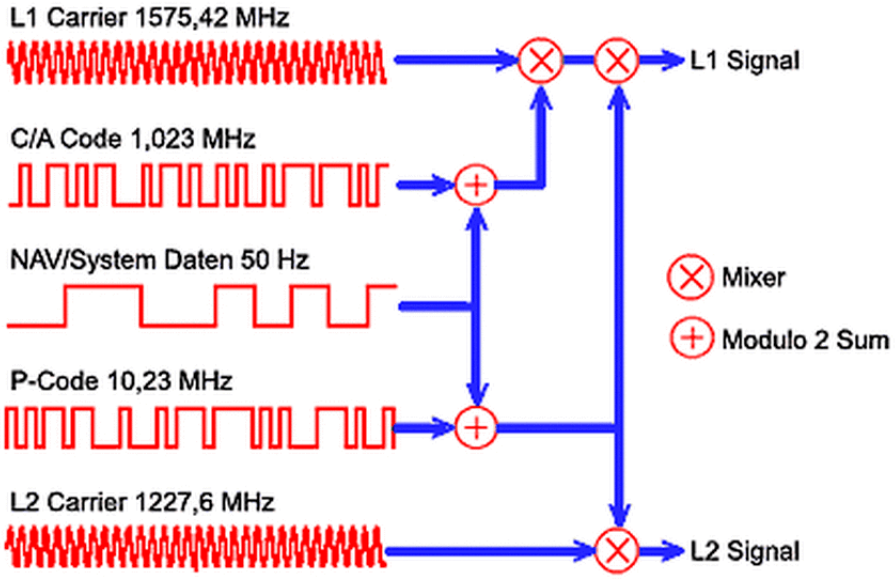

Figure 3.6: Modulation scheme for L1 and L2.

pseudorange) and this is why the GPS satellite's atomic clocks are used.

The synchronization error is calculated finding the pseudorange of an extra satellite, so the receiver needs three satellites for the computation of the position along x,y and z axis and another one for the time error Δt.
This means that the minimum number of satellites in sight that a receiver needs for a precise positioning process is four.

Pulse Per Second (PPS)

The Pulse Per Second (PPS) is an electrical signal that is repeated every second with an high precision. It is an output of precision clock devices, as the GPS system.
A PPS signal is used to synchronize computers and time measurement. This signal does not indicate the time (it simply marks the start of a second), in order to have a precise local time indication the PPS needs to be combined with a date and time source.

Currently the PPS accuracy in the GPS receiver is about 20 nanoseconds, a GPS receiver that works in single frequency contains a temperature controlled crystal oscillator which oscillates at 16MHz [26].

3.4.6 Sources of error

The major sources of GPS positional errors are [16]:

- Signal propagation errors
- Clock errors
- Ephemeris (orbital path) data errors
- Multi-path effects

The GPS satellites layout in the sky is another source that influence the accuracy of the positioning process, the optimal layout is an uniformed arrangement on a sphere around the receiver. When GPS satellites are close together in the sky, the positioning process suffers from Dilution Of Precision (DOP).

DOP values range from 1 (ideal case where there is no influence) to more than 20 (in which case, there is so much error the data should not be used). The DOP is defined as combination of different geometric components, the Horizontal Dilution Of Precision (HDOP) and the Vertical Dilution Of Precision (VDOP). The DOP related to the positioning is called Position Dilution Of Precision (PDOP, related to 3 spatial coordinates).
Since the orbital path of the GPS satellites is known, is possible to predict the PDOP for a given time and location.

3.5 Measurement errors

All the collected observations of satellite's position and velocity are affected by errors. The measurement error is defined as the variation of the observation respect the true value of the state vector. There are three main categories of errors:

- **Bias**, constant offset from the true value.
- **Noise**, statistical distribution of random variation around the measured mean value.
- **Drift**, unpredictable and slow variation of the observed mean value from the true value.

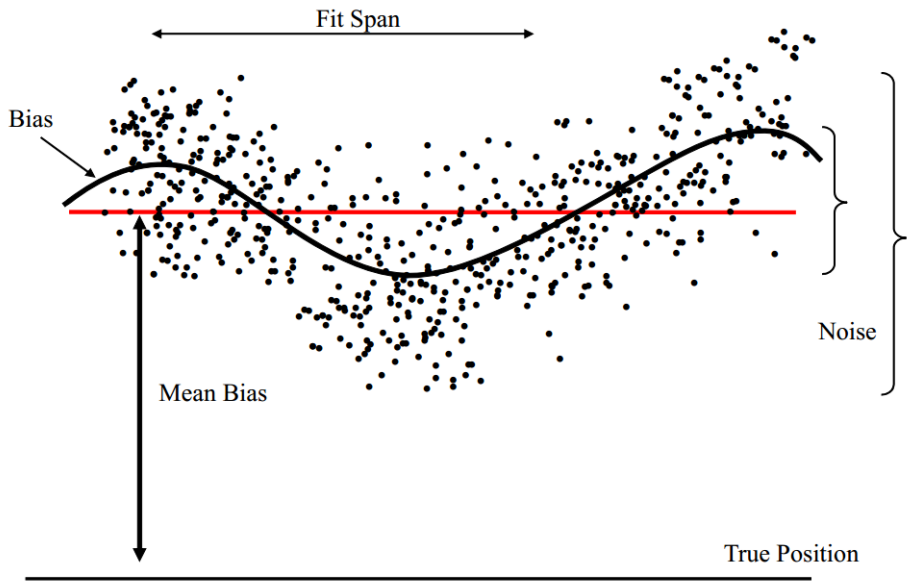

Figure 3.7: Representation of bias, noise and drift [27].

In Figure 3.7 there is a schematic representation of these errors: the mean of the observations has a bias from the true position, the variation around the mean value is the noise. Another kind of error is the variation of the bias over time respect to the average of the observations, this motion represent the changes in sensor performance and we can assume it as drift.
In order to compute the true position of a satellite different approaches could be used. In this work we will discuss the least-square analysis and the Kalman filtering.

Chapter 4

Developing and testing the localization filter

4.1 Requirements

The pulsar timing process objective is to detect the peaks of a millisecond pulsar. If the rotational period of the pulsar is about 1 ms and the peak has full width at half maximum (FWHM) of 1/10 of this period we need a timing accuracy of $\sim 30\ \mu s$, this will translate in a position accuracy of ~ 10 km. In order get a safety result, the maximum error on the position that we will accept is about 1 km.

This performance is easily reached using a GPS receiver. The filter corrections are required to smooth outliers on the GPS data, so hopefully it will give a decisive response only rarely during the mission.

4.2 Analysis of numerically generated data

To satisfy the positioning requirements of the mission, the performance of the *Fermi* NAV filter is taken as reference for the design of our positioning filter.

The work for the filter design was scheduled as follow:

1. Analysis of numerically generated data
    - Least square analysis
    - Kalman filter analysis

2. Analysis of real GPS data from *Fermi* telemetry

3. Comparison with the NAV filter

In order to compare our results to the *Fermi* NAV filter data, we tested the orbit determination processes on a numerically propagated orbit with the same orbital elements (OE) of *Fermi* mission.

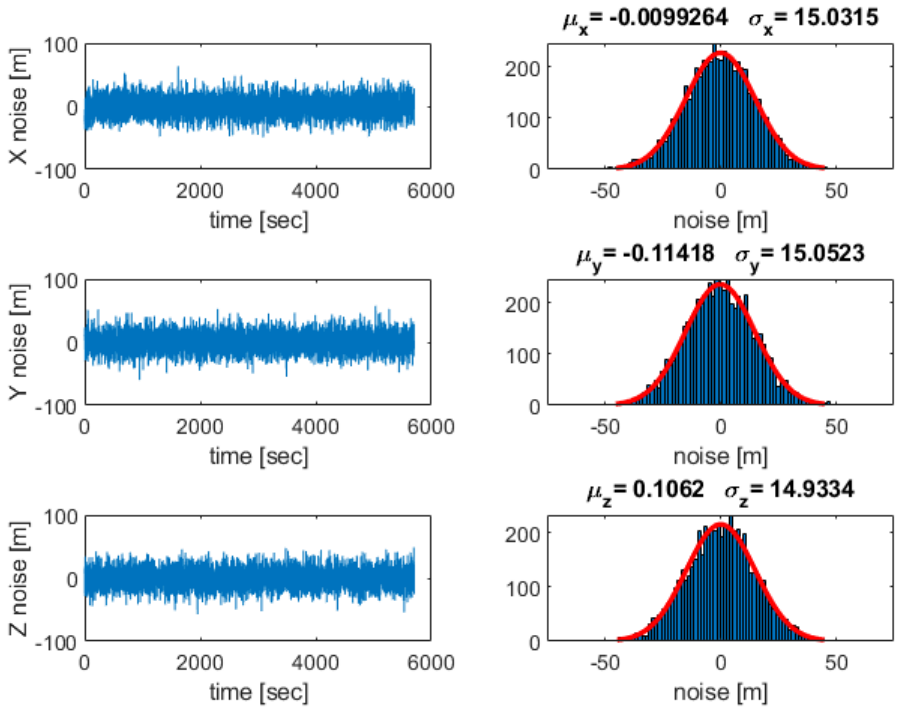

Figure 4.1: Position noise on the ideal orbit.

With a RK4 propagator we generated a reference orbit from a *Fermi* state vector using the J_4 model of motion described in Equation 3.3. Main OE of the propagated orbit are reported in Table 4.1.

As preliminary simulation the orbit is propagated for one period (T = 5702 sec). In order to simulate the GPS sensor performance, white noise with a zero mean is added on the simulation. In detail we added 15 m noise (1σ) on position and 0.1 m/s noise (1σ) on velocity, these values are given by the *Fermi* GPS data sheet

(Appendix). In Figure 4.1 is reported the position noise added on the three axes to the propagated orbit. In the next sections we will refer to the propagated orbit as "ideal orbit".

Eccentricity	0.001282
Semi-major axis	6912.9 km
Inclination	25.58 deg

Table 4.1: Main OE of the propagated orbit.

4.3 Least-Squares techniques

Least-Squares based algorithms are widely used in data fitting applications. The aim is to compute the best fit that minimize the sum of the squared residuals, where the residual is the difference between the fitted model and the observed data. The orbit determination is a nonlinear problem, so a Nonlinear Least-Squares (NLS) algorithm with differential correction was implemented following the [27] approach.

In order to understand why a NLS algorithm has a remarkable computational cost, we will give a focus on the calculation of the partial derivative matrix.

Partial derivative matrix

The partial derivative matrix, $\mathbf{A}$, describes how little variations in the initial state influence the computed positions. Given the initial state $\mathbf{X}_0$:

$$\mathbf{X}_0 = \begin{bmatrix} r_I & r_J & r_K & v_I & v_J & v_K \end{bmatrix} \qquad \mathbf{A} = \frac{\delta observations}{\delta \mathbf{X}_0}$$

$$\frac{\delta obs_i}{\delta \mathbf{X}_0} = \begin{bmatrix} \frac{\delta r_{I,i}}{\delta r_{I,0}} & \frac{\delta r_{I,i}}{\delta r_{J,0}} & \frac{\delta r_{I,i}}{\delta r_{K,0}} & \frac{\delta r_{I,i}}{\delta v_{I,0}} & \frac{\delta r_{I,i}}{\delta v_{J,0}} & \frac{\delta r_{I,i}}{\delta v_{K,0}} \\ \frac{\delta r_{J,i}}{\delta r_{I,0}} & \frac{\delta r_{J,i}}{\delta r_{J,0}} & \frac{\delta r_{J,i}}{\delta r_{K,0}} & \frac{\delta r_{J,i}}{\delta v_{I,0}} & \frac{\delta r_{J,i}}{\delta v_{J,0}} & \frac{\delta r_{J,i}}{\delta v_{K,0}} \\ \frac{\delta r_{K,i}}{\delta r_{I,0}} & \frac{\delta r_{K,i}}{\delta r_{J,0}} & \frac{\delta r_{K,i}}{\delta r_{K,0}} & \frac{\delta r_{K,i}}{\delta v_{I,0}} & \frac{\delta r_{K,i}}{\delta v_{J,0}} & \frac{\delta r_{K,i}}{\delta v_{K,0}} \end{bmatrix}$$

$\mathbf{A}$ is calculated using the finite differencing method (the term δ_i represent the variation of the initial state's parameters):

$$\frac{\delta observations}{\delta \hat{\mathbf{X}}_0} \cong \frac{f(\hat{\mathbf{X}} + \delta_i) - f(\hat{\mathbf{X}})}{\delta_i}$$

The steps of the finite differencing algorithm are:

1. Orbital propagation from the nominal initial state to the state at time "t_i":

$$r_{nom}, v_{nom}, \Delta t_i \quad \rightarrow \quad r_i, v_i$$

2. For j = 1 to 6 (number of the state parameters)
   Introduction of a little variation (1% of the nominal value) on the parameter j:

$$\delta_j = \hat{\mathbf{X}}_{nom,j} \cdot (0.01) \quad \rightarrow \quad \delta_j = \hat{\mathbf{X}}_{nom,j} + \delta_j$$

3. Orbital propagation from the modified initial state:

$$r_{mod}, v_{mod}, \Delta t_i \quad \rightarrow \quad r_i, v_i$$

4. Computation of the j-column of the **A** matrix:

$$\frac{\delta obs_j}{\delta_j} = \frac{obs_{mod} - obs_{nom}}{\delta_j}$$

5. Reset of $\hat{\mathbf{X}}_{mod,j}$ to its nominal value and restart the loop with the next j value.

This loop has to be computed for every measured data. Assuming that a set of data is composed by "n" observations, a number of "$6 \cdot n$" numerical integration of motion are required for each iteration until the convergence is reached.
This amount of numerical integration processes has an important computational cost, for this reason the NLS method is recommended for *a posteriori* (on ground) analysis of the spacecraft position.

Due to the limitation of computing performance on a satellite's CPU, it is not advisable to run effectively a NLS code for real time orbit determination.

4.4 NLS application

The NLS application for orbit determination is quite simple. As described previously, the [27] approach was implemented.

The principle of this application is to find the best estimate of the initial state vector that minimize the squared residuals between a computed orbit and the observed position. The optimized initial state is obtained from differential correction to each parameter (x y z position and x y z velocity), in Figure 4.2 an example is reported of the position correction trend over iterations for a simulation of one orbit.

In order to analyze the performance of the NLS algorithm, different data sampling intervals were tested. The reference set up for the simulation has 1 s of sampling

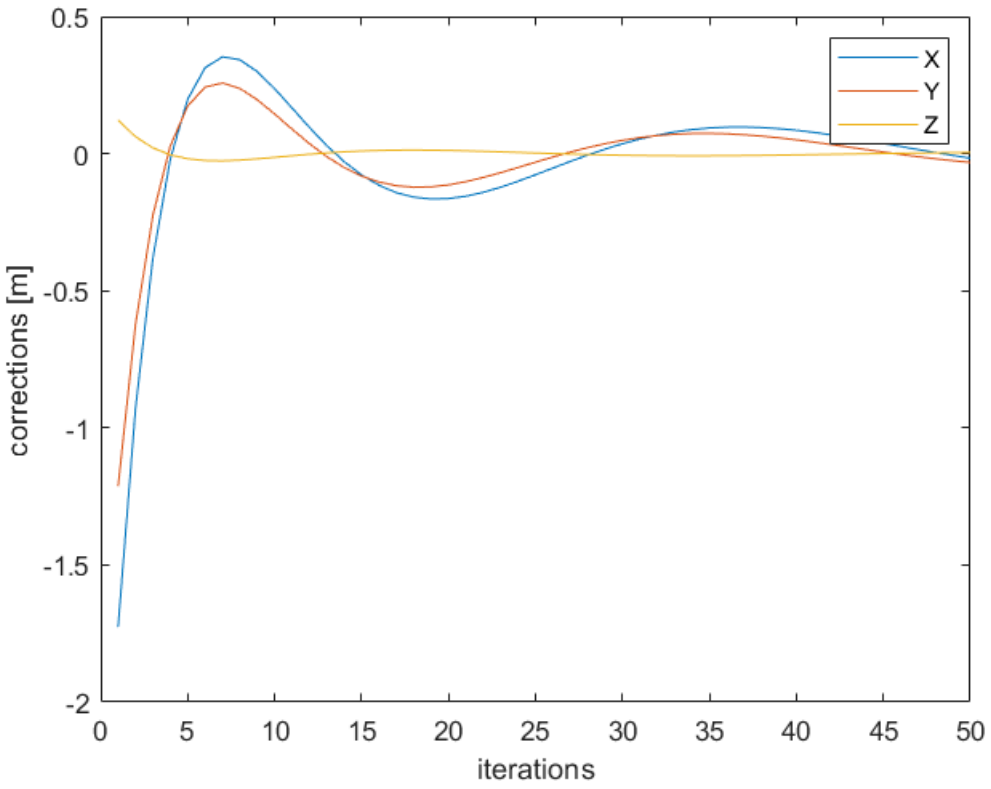

Figure 4.2: Example of position corrections on the initial State Vector.

interval for 1 orbit simulation, so we have a batch of data composed by almost 5700 states.

The results of this simulation are impressively good. As reported in Figure 4.3, the computed position along the three axes is included between ± 1 m error from the ideal orbit.

The results of the NLS analysis are strongly related to accuracy of the model of motion used for the orbital propagation, if the model diverges from the reality the computed position will drift from the ideal and errors will arise.
Due to the differences between the orbital models with and true motion, the analysis of real data using NLS can not be done for a long time-span (our NLS simulations on the numerically generated data use a J_4 orbital model that is the same used for the ideal orbit propagation and this is an optimal case).

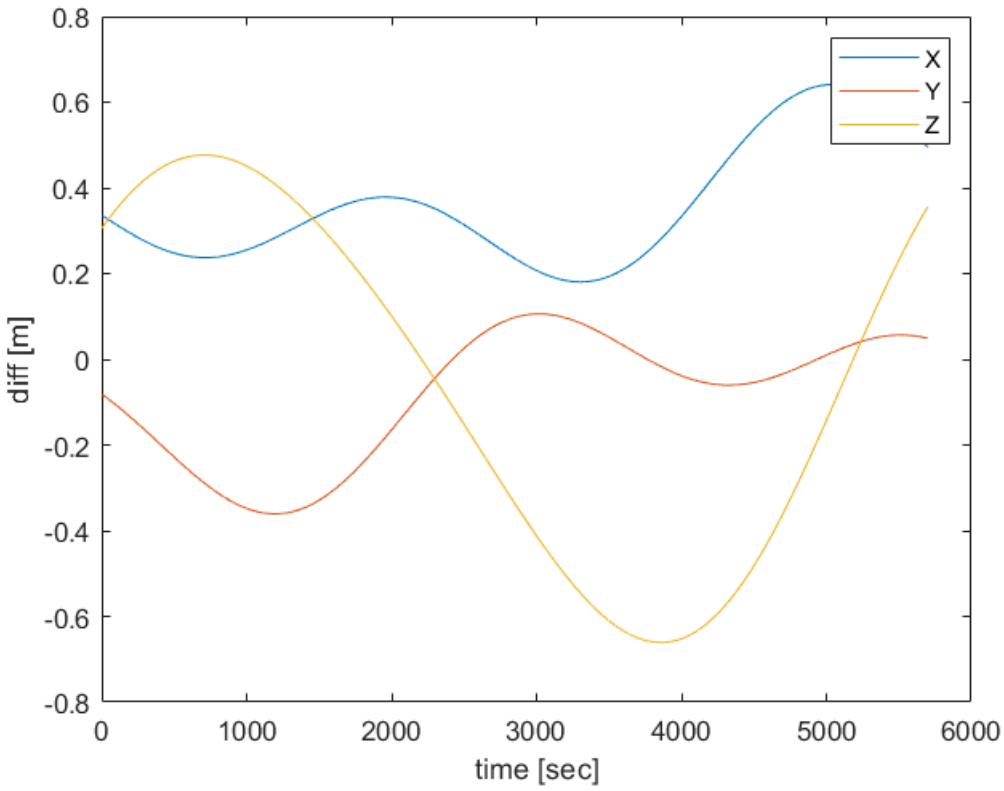

Figure 4.3: Differences between the computed orbit and the ideal orbit over time.

In addition to the influence of the model of motion implemented, we find a dependence of the solution accuracy from the initial condition knowledge. Good precision on the initial state vector will help a lot the convergence speed of the method and its solution accuracy.

4.5 Kalman filtering

The Kalman filter was developed for the trajectory estimation of the Apollo program spacecrafts. It takes its name from its inventor, Rudolf Kalman.

This filter uses a set of measurements affected by Gaussian noise to valuate the best estimate of a system status based on a system model.

We can define the problem as:

$$\mathbf{X}_k = \mathbf{\Phi}_s \cdot \mathbf{X}_{k-1} + \epsilon_{k-1}$$
$$\mathbf{Y}_k = \mathbf{H}_k \cdot \mathbf{X}_k + \mathbf{v}_k$$

Where:

- $\mathbf{X}$ = State vector
- k = instant of time in valuation
- $\mathbf{\Phi_s}$ = State transition matrix
- ϵ = State determination noise
- $\mathbf{Y}$ = Measurement vector
- $\mathbf{H}$ = Measurement matrix
- $\mathbf{v}$ = Measurement noise

For noise and error evaluation we define the matrices $\mathbf{Q}$ (Covariance matrix of the state model), $\mathbf{R}$ (Covariance matrix of the measurement noise) and $\mathbf{P}$ (Covariance matrix of the state valuation).
The algorithm works in two main phases:

1. Prediction of the State vector at time "$k+1$" from the State at time "k"
2. Correction of the State vector at time "$k+1$" using the measurement at "$k+1$"

As reference, the over-line on a term denotes a predicted term. Terms with hat are corrected.

Prediction

As first phase we will compute a predicted state $\overline{\mathbf{X}}_{k+1}$ and a predicted error covariance $\overline{\mathbf{P}}_{k+1}$ at time "$k+1$".

$$\begin{aligned} \overline{\mathbf{X}}_{k+1} &= \mathbf{\Phi}_s \hat{\mathbf{X}}_k && \text{Predicted State} \\ \overline{\mathbf{P}}_{k+1} &= \mathbf{\Phi} \hat{\mathbf{P}}_k \mathbf{\Phi}^T + \mathbf{Q} && \text{Predicted Error Covariance} \end{aligned}$$

Correction

As second phase we will correct the predicted state. The corrected state comes from a trade off between the predicted and the measured state, this operation is based on the Kalman Gain "$\mathbf{K}$".
The Kalman Gain denotes how much we trust the measure compared to the prediction model. The terms of $\mathbf{K}$ are between 0 and 1: if $K \to 0$ we trust the model prediction, otherwise if $K \to 1$ we trust the measurement.
The steps of the correction phase are:

$$\begin{aligned} \mathbf{K}_{k+1} &= \overline{\mathbf{P}}_{k+1} \mathbf{H}^T [\mathbf{H} \overline{\mathbf{P}}_{k+1} \mathbf{H}^T + \mathbf{R}]^{-1} && \text{Kalman Gain computation} \\ \hat{\mathbf{X}}_{k+1} &= \overline{\mathbf{X}}_{k+1} + \mathbf{K}_{k+1} [\mathbf{Y} - \mathbf{H} \overline{\mathbf{X}}_{k+1}] && \text{State Estimate} \\ \hat{\mathbf{P}}_{k+1} &= [\mathbf{I} - \mathbf{K}_{k+1} \mathbf{H}] \overline{\mathbf{P}}_{k+1} && \text{Error Covariance Estimate} \end{aligned}$$

These two phases are repeated in loop using the State and the Error Covariance Estimate at "$k+1$" as starting point for the next iteration.

4.5.1 Model

For our application we will use a 3d constant acceleration model of motion.
The State vector $\mathbf{X}$ is a 9x1 element defined as:

$$\mathbf{X}^T = [r_x r_y r_z v_x v_y v_z a_x a_y a_z]$$

According to the acceleration dynamic model, we find velocity and acceleration by knowing acceleration and integrating:

$$\begin{aligned} a(t) &= a_0 \\ v(t) &= v_0 + a_0 \Delta t \\ r(t) &= r_0 + v_o \Delta t + \frac{1}{2} a_0 \Delta t \end{aligned}$$

Or in the matrix form for the three axis:

$$\mathbf{\Phi} = \begin{bmatrix} 1 & 0 & 0 & \Delta t & 0 & 0 & \frac{\Delta t^2}{2} & 0 & 0 \\ 0 & 1 & 0 & 0 & \Delta t & 0 & 0 & \frac{\Delta t^2}{2} & 0 \\ 0 & 0 & 1 & 0 & 0 & \Delta t & 0 & 0 & \frac{\Delta t^2}{2} \\ 0 & 0 & 0 & 1 & 0 & 0 & \Delta t & 0 & 0 \\ 0 & 0 & 0 & 0 & 1 & 0 & 0 & \Delta t & 0 \\ 0 & 0 & 0 & 0 & 0 & 1 & 0 & 0 & \Delta t \\ 0 & 0 & 0 & 0 & 0 & 0 & 1 & 0 & 0 \\ 0 & 0 & 0 & 0 & 0 & 0 & 0 & 1 & 0 \\ 0 & 0 & 0 & 0 & 0 & 0 & 0 & 0 & 1 \end{bmatrix} \tag{4.1}$$

The measurements are provided by the satellite's GPS receiver, it give us position measurements (r_x, r_y, r_z) and velocity measurements (v_x, v_y, v_z). The measurement matrix will be:

$$\mathbf{H} = \begin{bmatrix} 1 & 0 & 0 & 0 & 0 & 0 & 0 & 0 & 0 \\ 0 & 1 & 0 & 0 & 0 & 0 & 0 & 0 & 0 \\ 0 & 0 & 1 & 0 & 0 & 0 & 0 & 0 & 0 \\ 0 & 0 & 0 & 1 & 0 & 0 & 0 & 0 & 0 \\ 0 & 0 & 0 & 0 & 1 & 0 & 0 & 0 & 0 \\ 0 & 0 & 0 & 0 & 0 & 1 & 0 & 0 & 0 \end{bmatrix} \tag{4.2}$$

The covariance matrix of the measurements noise ($\mathbf{R}$) depends on the performance of the measurement sensors. It is a diagonal matrix with terms related to the accuracy of position measurements ($\sigma_{Px}, \sigma_{Py}, \sigma_{Pz}$) and velocity measurements ($\sigma_{Vx}, \sigma_{Vy}, \sigma_{Vz}$).

$$\mathbf{R} = \begin{bmatrix} \sigma_{Px}^2 & 0 & 0 & 0 & 0 & 0 \\ 0 & \sigma_{Py}^2 & 0 & 0 & 0 & 0 \\ 0 & 0 & \sigma_{Pz}^2 & 0 & 0 & 0 \\ 0 & 0 & 0 & \sigma_{Vx}^2 & 0 & 0 \\ 0 & 0 & 0 & 0 & \sigma_{Vy}^2 & 0 \\ 0 & 0 & 0 & 0 & 0 & \sigma_{Vz}^2 \end{bmatrix} \tag{4.3}$$

4.6 Kalman filter application

4.6.1 Kinematic model errors

We implemented the Kalman filter with a "Kinematic model" described by Equation 4.1, but the orbital motion is a non linear problem. This assumption introduces an error that depends on the sampling interval.

The error trend on the three axes depends also from the satellite's velocity: when the velocity on an axis is small also the error become little. To get an idea of the error magnitude we can simply compute it from the propagated orbit, as:

$$Error = Position(t = k) + Velocity(t = k) \cdot dt - Position(t = k + 1) \tag{4.4}$$

In Figure 4.4 is reported the trend of the errors due to a sampling time of 1 second. As we can see, the errors on the three axes have a sinusoidal trend that follow the velocity but the norm of the errors is almost constant around 4.18 meters.

4.6.2 Q and R matrix

As we described in Section 4.5 the **Q** matrix is the covariance matrix of the state model and it represent the error of the motion model. In our case **Q** can be tuned using the errors on position and velocity computed like in Section 4.6.1.
We followed an alternative way, to construct **Q** we treated the covariance model as the 3rd derivatives of the satellite's positions (da/dt) as zero-mean random variables (jerk) with known variances, σ_{Jx}, σ_{Jy} and σ_{Jz}.

The **R** matrix components are set from the GPS receiver performance. According to the *Fermi* GPS datasheet (Section 6.1), we will set:

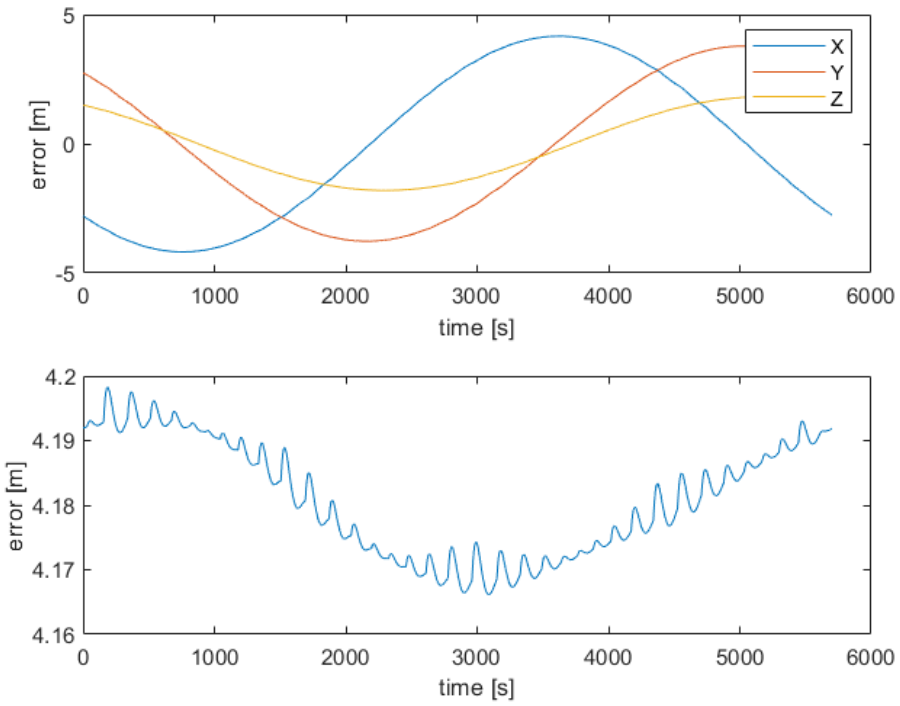

Figure 4.4: Error due to the 1 sec kinematic model on the three axes and it's norm.

$$\mathbf{R} = \begin{bmatrix} (15)^2 & 0 & 0 & 0 & 0 & 0 \\ 0 & (15)^2 & 0 & 0 & 0 & 0 \\ 0 & 0 & (15)^2 & 0 & 0 & 0 \\ 0 & 0 & 0 & (0.1)^2 & 0 & 0 \\ 0 & 0 & 0 & 0 & (0.1)^2 & 0 \\ 0 & 0 & 0 & 0 & 0 & (0.1)^2 \end{bmatrix} \tag{4.5}$$

4.6.3 Different sampling frequencies

As we said in Section 4.6.1, different sampling frequencies lead to different errors on the model. In order to estimate the optimal sampling interval we have analyzed different solutions, in detail the sampling interval tested are: 0.5, 0.75, 1, 2, 3, 5, 10, 15 seconds.

The results are reported in Figures 4.5, 4.6, 4.7, 4.8. It is clearly visible that with the increasing of the time span between the observations the filter's performance drops.

As we can in see in Figure 4.5 for 15 and 10 seconds intervals, the performance of the filter is the same of the GPS sensor. This fact is due to the error of the kinematic model that becomes grater than the sensor's noise and the filter trusts the observations more than the model prediction.

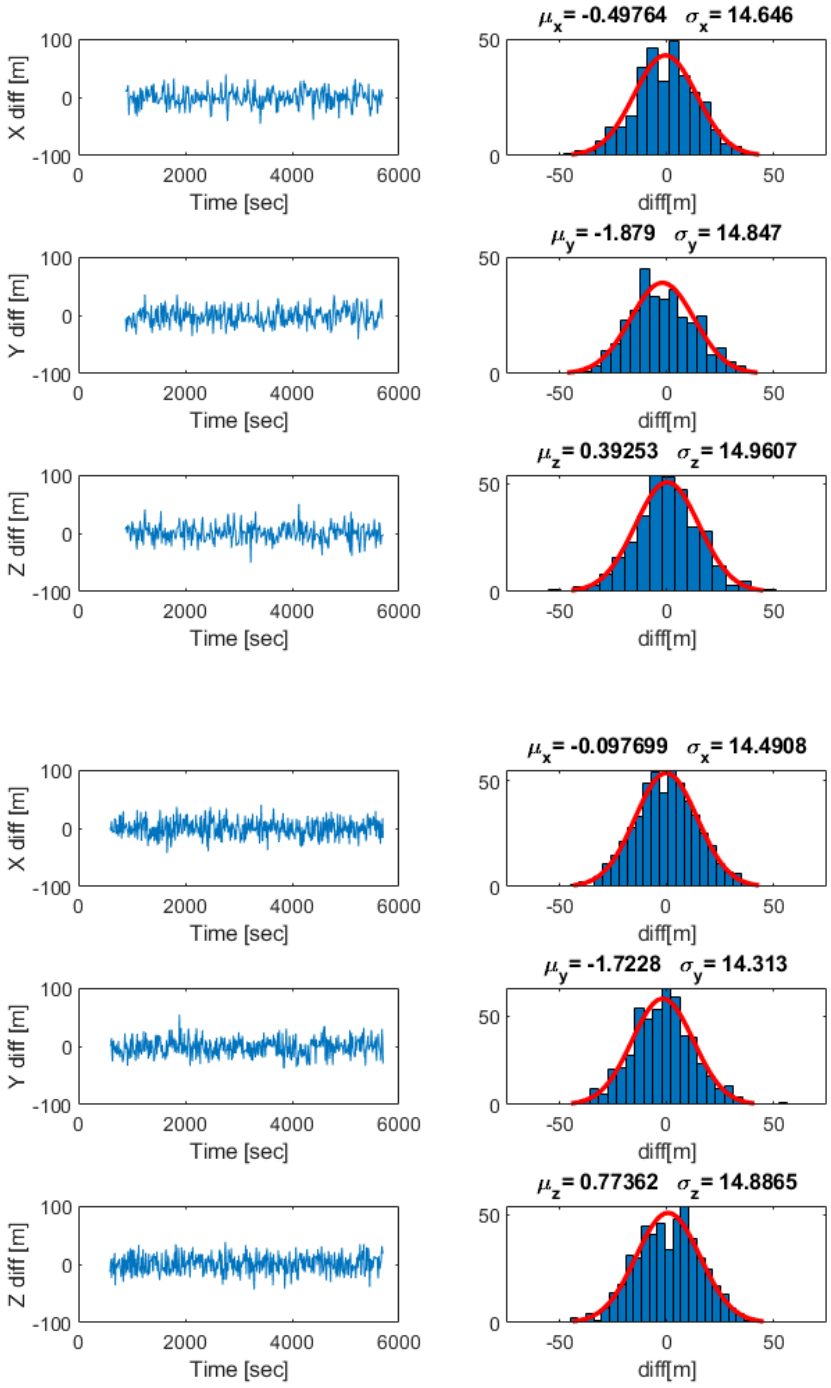

Figure 4.5: 15 and 10 seconds sampling time filter performance.

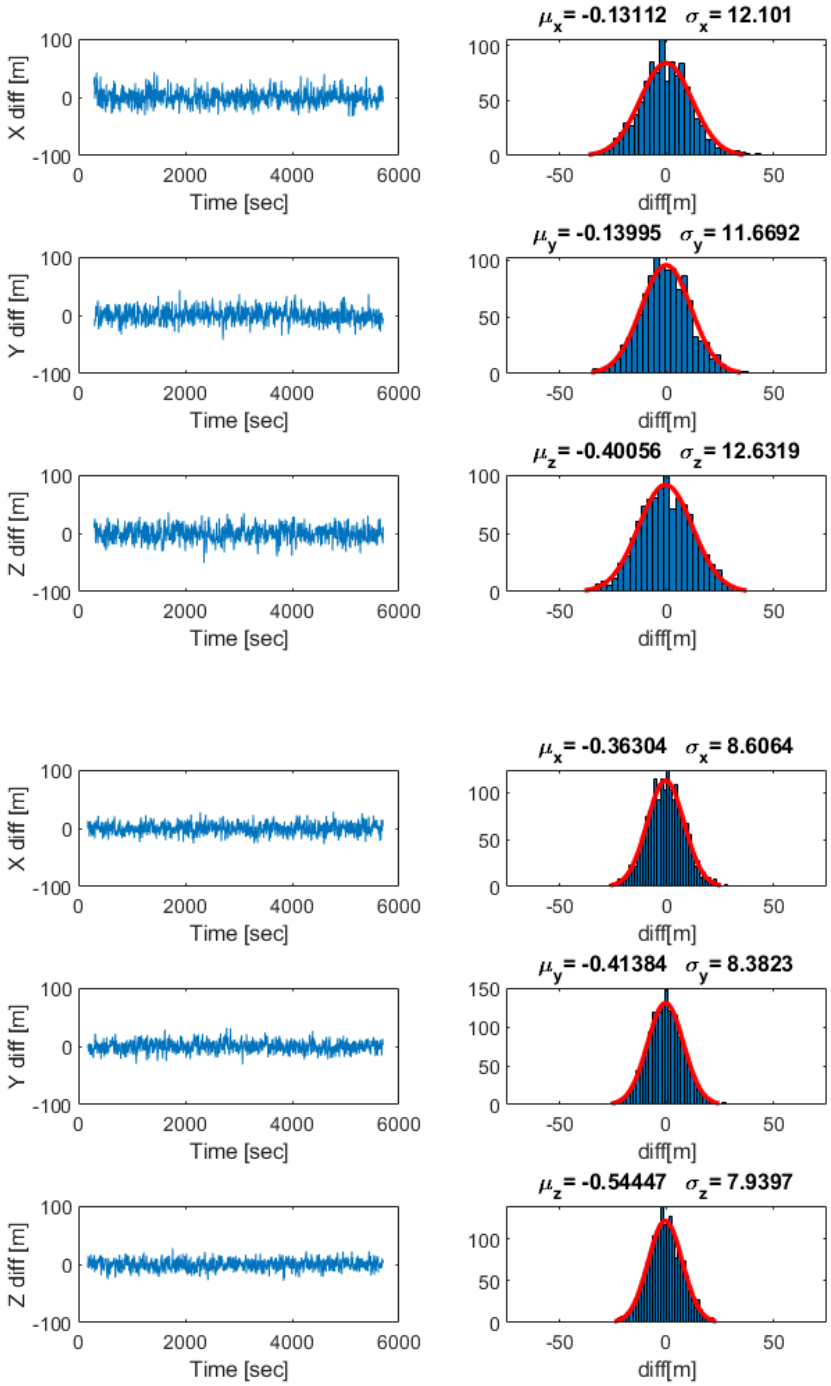

Figure 4.6: 5 and 3 seconds sampling time filter performance.

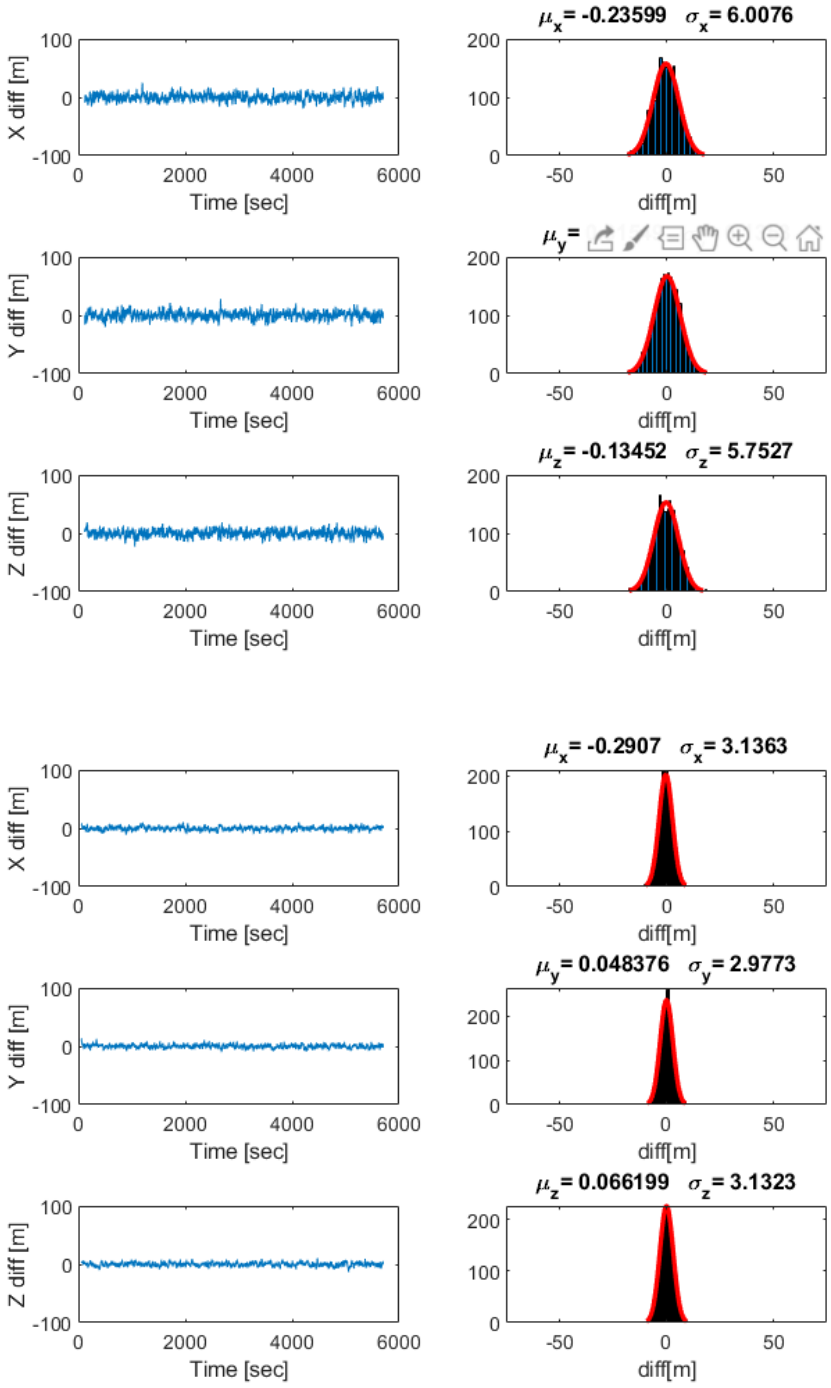

Figure 4.7: 2 and 1 seconds sampling time filter performance.

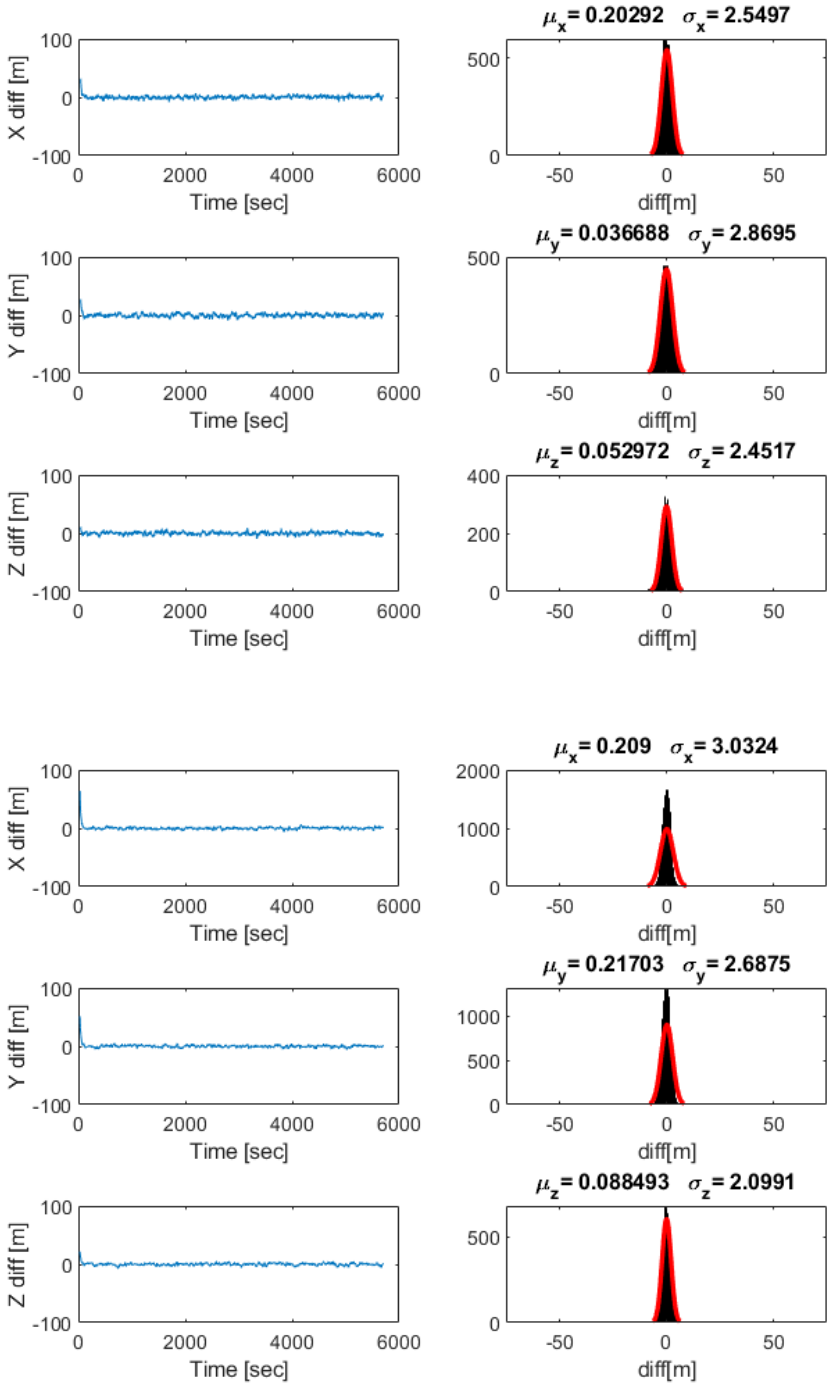

Figure 4.8: 0.75 and 0.5 seconds sampling time filter performance.

4.6.4 Outlier events

Once we have tested the performance of the filter under Gaussian distributed errors, we now evaluate its behavior when we introduce one much larger position error (outlier). This kind of errors will be described in Section 4.9, they can be induced in the telemetry e.g. by an erroneous association of a time with a measured position. In a LEO orbit a satellite flies with a speed of ~ 7 km/s, it means that a time-stamping error of 0.5 second would be seen as a position error of about ~ 3.5 km.

In order to simulate these outliers we introduce in our noise model a large position error with a magnitude of 100 times the standard deviation σ. In Figure 4.9 the comparison of the position residuals with and with out the filter is reported. As we can see the filter performance is good, it allows to smooth the bad position with a residual that is one order of magnitude better than the original.

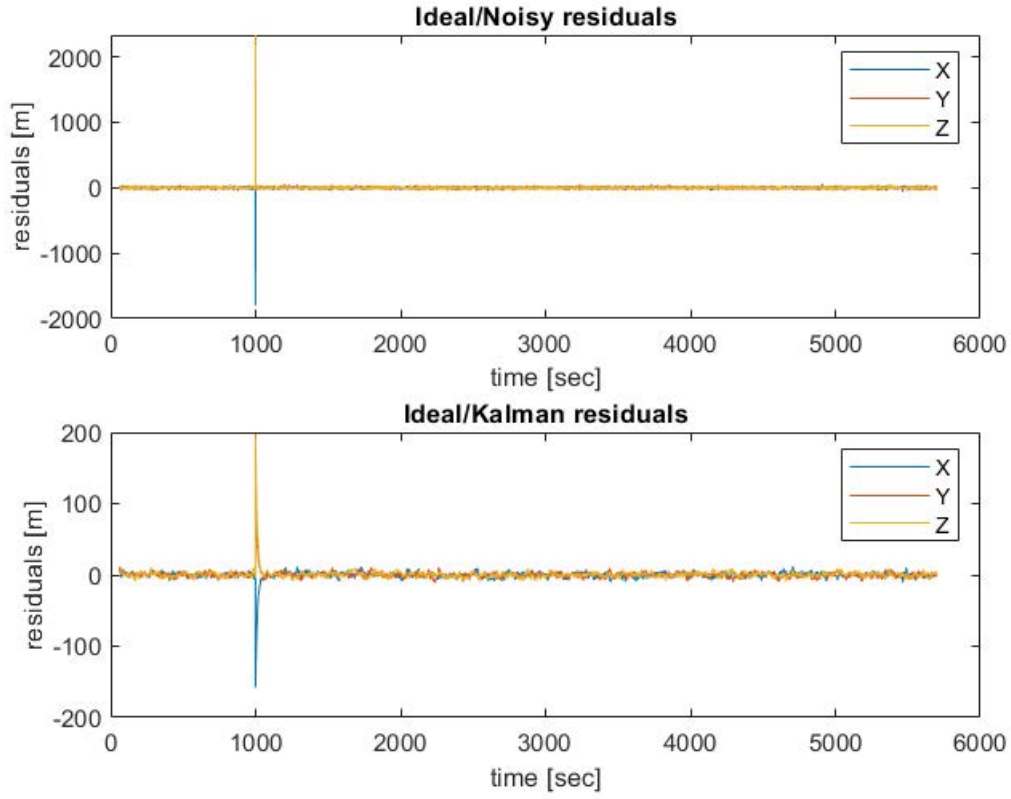

Figure 4.9: High position error (above) and relative filter performance (below).

In Figure 4.10 there is a focus on the correction. After the bad position data the filter takes a little settling time to reach again the optimal performance.

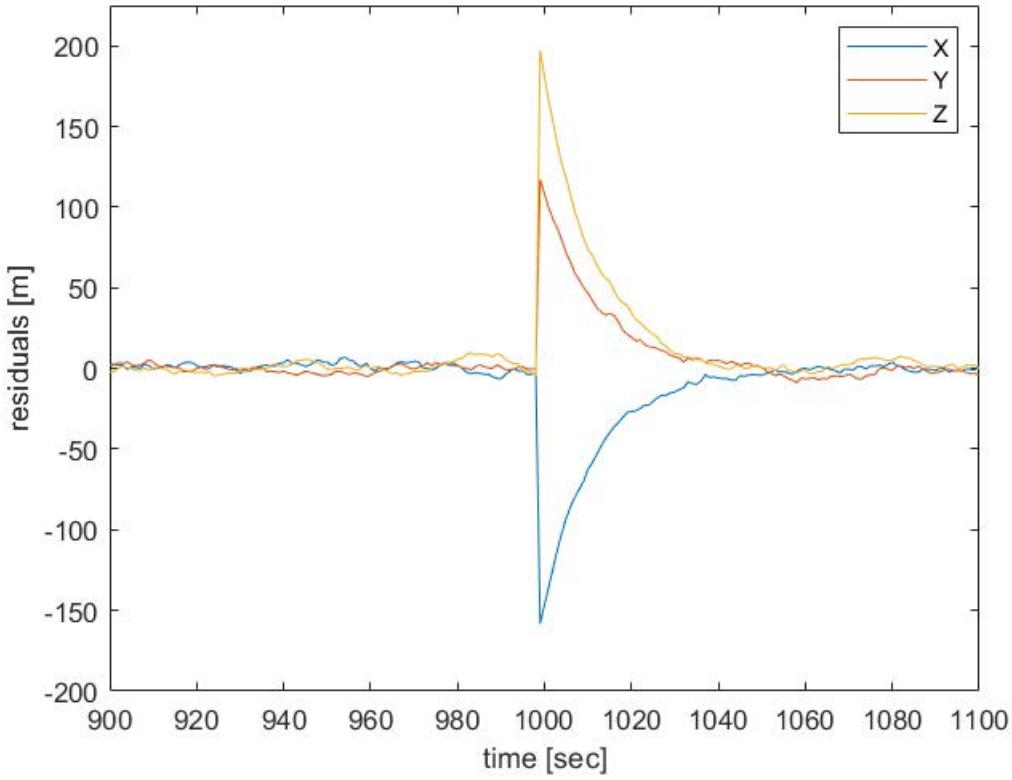

Figure 4.10: Detail of the high position error correction.

4.7 *Fermi* position data analysis

Due to the NLS high computational cost and to uncertainties on the orbit model we decided to test only the Kalman filter. The analysis of the filter performance on the *Fermi* telemetry data was based on a time interval of a month, from UTC time `'2016-12-31 23:30:01.540099'` to `'2017-02-01 00:29:59.940076'` (1 month selected at random plus 30' padding at either end).

Parameter	**Units**	**Description**
Telemetry packets time	string	UTC Time
GPS clock	seconds	GPS Time
NAV clock	seconds	Mission Elapsed Time
GPS position X	meters	ECEF Position
GPS position Y	meters	ECEF Position
GPS position Z	meters	ECEF Position
GPS velocity X	meters/seconds	ECEF velocity
GPS velocity Y	meters/seconds	ECEF velocity
GPS velocity Z	meters/seconds	ECEF velocity
NAV position X	meters	ECI J2000 Position
NAV position Y	meters	ECI J2000 Position
NAV position Z	meters	ECI J2000 Position
NAV velocity X	meters/seconds	ECI J2000 velocity
NAV velocity Y	meters/seconds	ECI J2000 velocity
NAV velocity Z	meters/seconds	ECI J2000 velocity
Squared residuals NAV/GPS	meters^2	(optional output)

Table 4.2: Selected *Fermi* telemetry outputs.

The outputs that we selected from the *Fermi* telemetry database are reported in Table 4.2 (internal data, courtesy of the *Fermi* LAT Collaboration). The GPS location is given in an ECEF reference system, the output of the navigation Filter on board (NAV) is given in an ECI reference system, as required by the science analysis software. LAT times are given as MET (Mission Elapsed Time), seconds elapsed from 2001-01-01 00:00:00 UTC. The GPS Time is similar, but does not account for leap seconds. Each telemetry packet is timestamped with its UTC time string, frequency is approximately 2 packets per seconds.

The selected data from the telemetry stream were dumped into a `.csv` file composed by 5809824 points, for a dimension of 1.13 GB. The telemetry packets are sent quite frequently and out-of-sync with either NAV and GPS clocks, so each location is reported in the file two or more time, with a different telemetry time-stamp, so we developed a data selector in order to extract and clean the data of interest for our application.

As we have discussed, using the telemetry stream adds some additional complications and require some data selection and cleaning that would not arise if working on the on board CPU and accessing the NAV and GPS registers.

4.8 Results

During the analysis of *Fermi* telemetry the filter recognizes correctly the two kinds of error that we tested with the numerically propagated orbit.

The differences between these errors are clearly visible. As reported in Figure 4.11, errors due to the sensor noise produce tens of meters residuals from the GPS measured position.

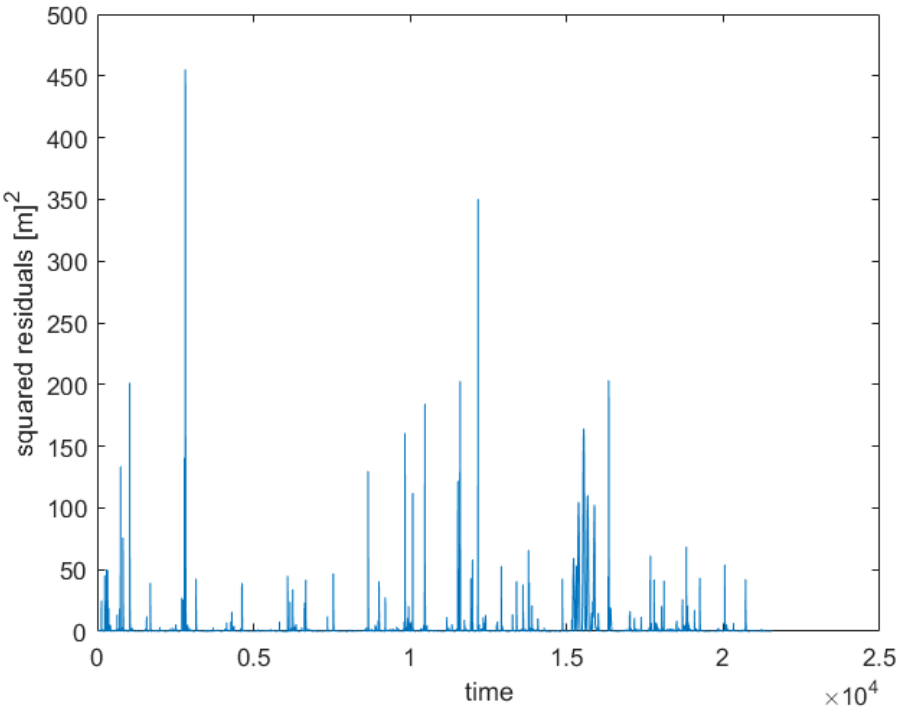

Figure 4.11: Example of correction of sensor noise.

Note: The time reported on the plots is normalized respect the time of the first point of the examined `.csv` file.

As expected, errors due to outliers are detected and smoothed. In Figure 4.12 it is possible to see that the corrections have an huge magnitude compared to GPS noise. In the example we show, peaks are smoothed and they present squared residuals of $\approx 2.5 \cdot 10^7\ m^2$ (around 5 km error). It means that this would translate into a timing error of ≈ 0.8 s.

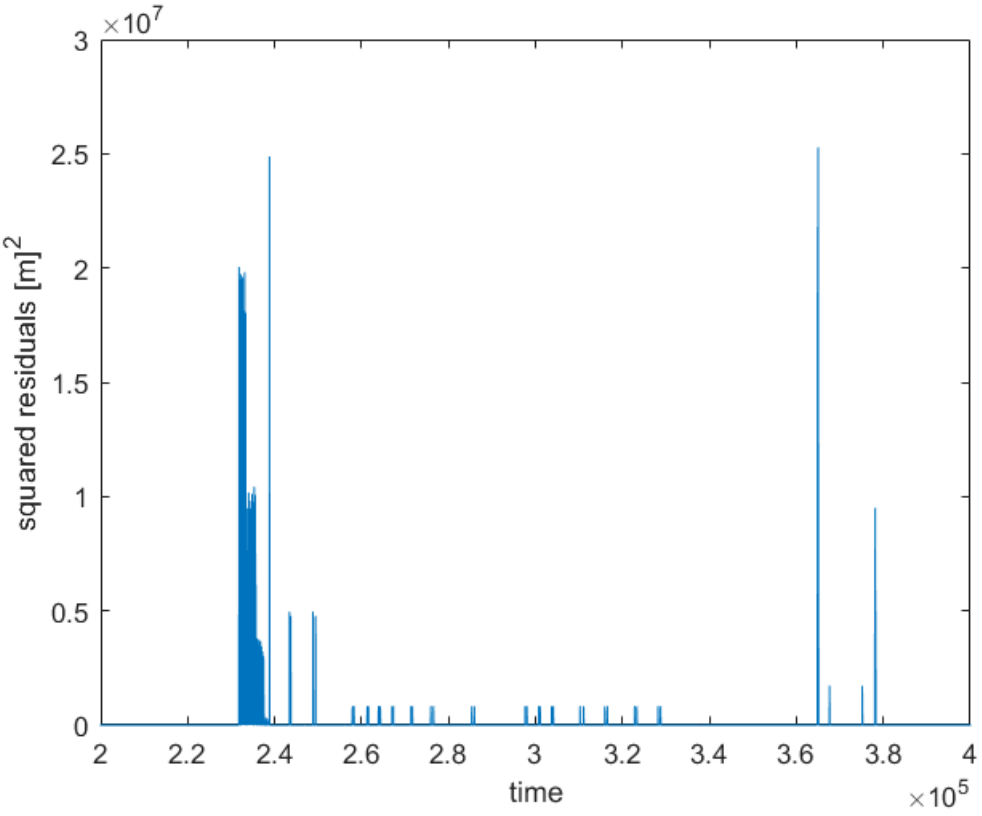

Figure 4.12: Example of errors due to outliers.

Compared to the *Fermi* corrected NAV data, the performance of our filter is good and it achieves comparable results on errors detection and error smoothing.

An interesting result is reported in in Figure 4.13, in this plot we show a comparison between the two filters. As we can see the in house filter detects and corrects a position error peak of ≈ 9 meters with a performance close to the NAV. Our filter detects also a pattern of periodical small recurrent deviations of about 6 m, which we do not understand but are inconsequential.

To try to understand this behaviour of the filters, we checked the NAV data and discovered that the discrepancies we observe are not detected explicitly by the NAV filter, i.e. they do not appear in the reported squared residuals output, but appear to be corrected in the right way nonetheless.

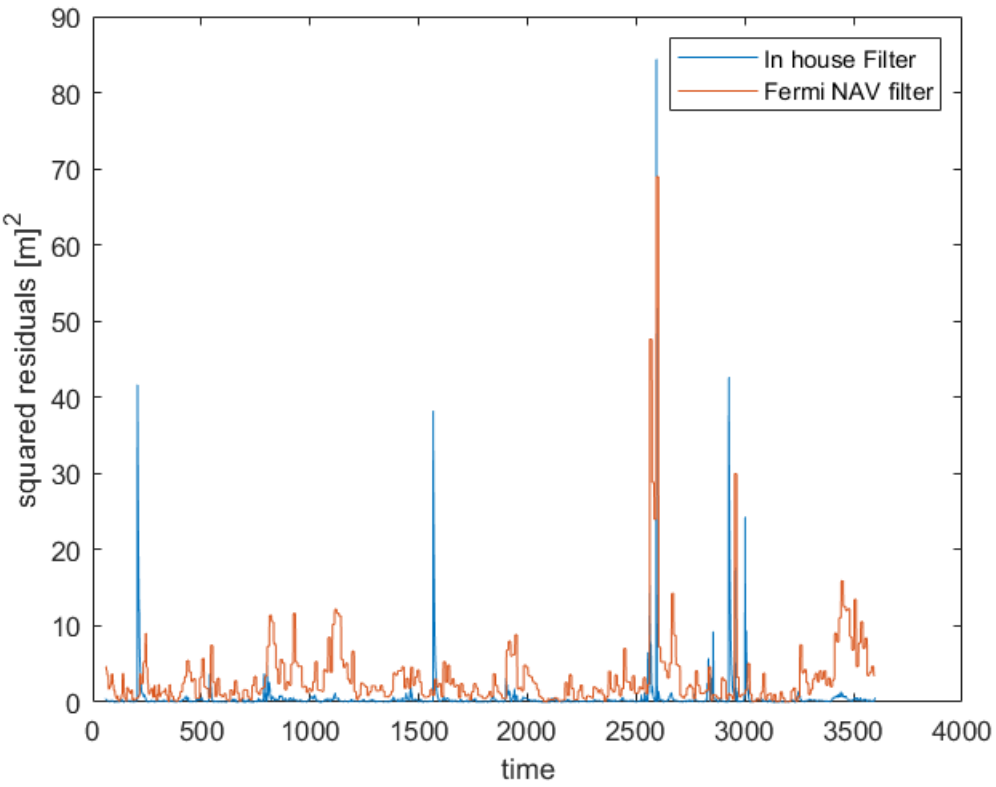

Figure 4.13: Comparative plot between the in house and the NAV filter.

From Figure 4.13 is also possible to notice that our filter produces less residuals most of the time, this means that we follow the GPS more than the NAV, which smooths more.

4.9 Investigation of the outliers

To understand the nature of the outliers we investigated the datastream with great attention looking for artefacts.

One source of errors was related to the introduction of the leap second between `2016-12-31 23:59:59` and `2017-01-01 00:00:00`.

Then we noticed that in some case the telemetry reads the registers while they are being updated, so we can have two packets containing e.g. the same GPS location while the GPS time is already incremented, or the opposite. This causes a large apparent error in the location, and we had to tag and remove all such events. With a dedicated data selector code we handled the multiplicity of positions and timestamps as exceptions. In Table 4.3 is reported a typical outlier characterized by two different positions for the same timestamp.

UTC time	MET	GPSposY	GPSposX	GPSposZ
'2017-01-03 16:18:46.000'	505153131	5523137.58	4031817.52	-1056494.98
'2017-01-03 16:18:48.000'	505153133	5519727.87	4037285.64	-1053427.44
'2017-01-03 16:18:48.000'	505153133	5516312.38	4042749.46	-1050358.70
'2017-01-03 16:18:49.000'	505153134	5512890.92	4048208.86	-1047288.55
'2017-01-03 16:18:50.000'	505153135	5509463.61	4053663.90	-1044217.10

Table 4.3: Detail of a typical outlier.

So it turns out that in order to simulate the performance of the filter as it would be running on a CPU, so with no artefacts, we had to operate an "outlier cleaning process" on the telemetry data.

In Figure 4.14 we report the squared residuals of the filter corrections over the month of valuation after this cleaning process. Compared to the focus on the outliers correction (Figure 4.12), is clearly visible that the filter finds only errors due to the GPS noise.

This result is even more evident looking the distribution of the corrections reported in Figure 4.15 and Figure 4.16.

The first plot reports the distribution of the corrections in the case of a file with outliers, as we can see it presents a lot of corrections with a magnitude of ≈ 1000 meters and a tail with magnitude around 6000 meters.

The second plot reports the case of the telemetry cleaned from the outliers. As expected the distribution looks like a decreasing exponential, with most corrections within 60 meters and few cases from 60 to 160 meters.

In conclusion of our investigation, large outliers are just artefacts of the telemetry

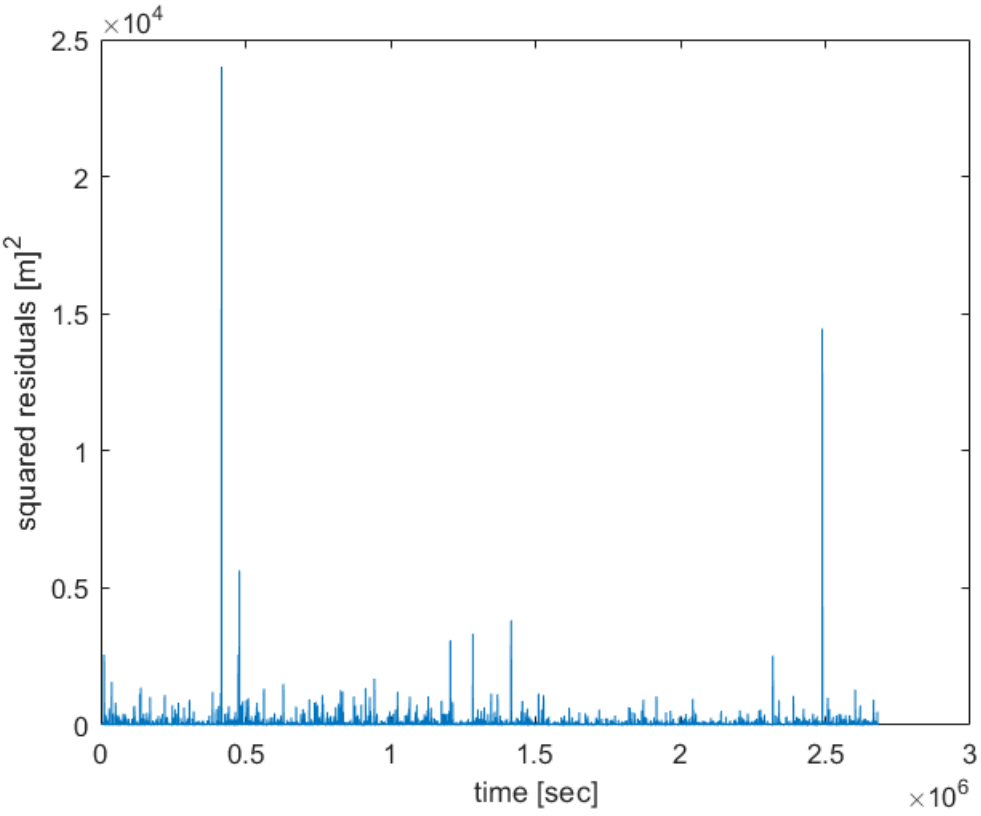

Figure 4.14: Corrections on the GPS measured position without outliers.

stream and can be removed with a cleaning process.

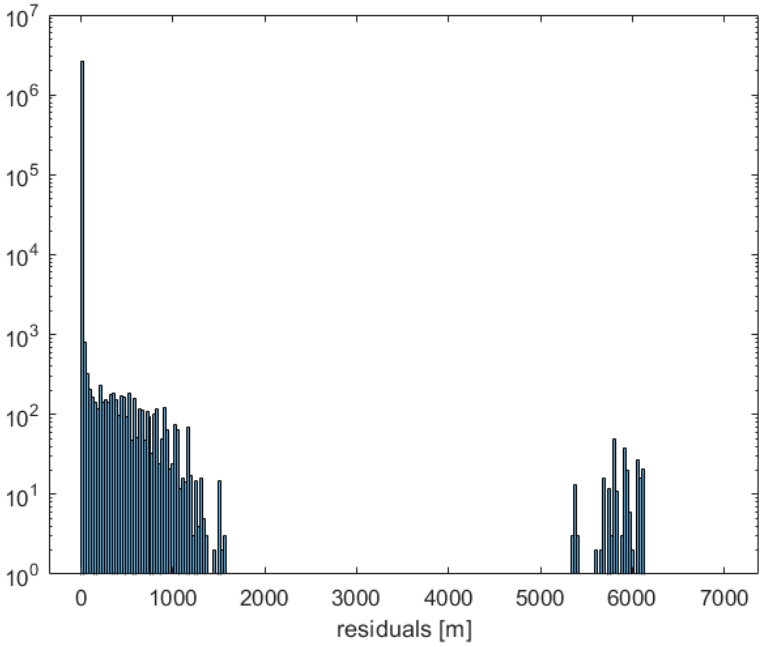

Figure 4.15: Correction distribution on a telemetry file with outliers.

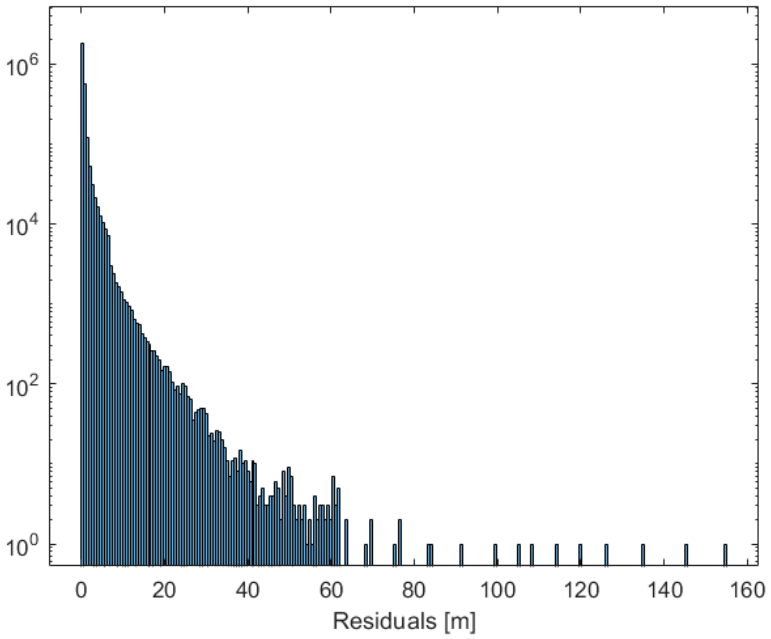

Figure 4.16: Correction distribution of data in Figure 4.14.

Chapter 5

Verification with pulsar timing

5.1 `ft1` file

As told previously, in Section 2.5, the `ft1` file contains the data of the photons detected by *Fermi* LAT. This input file is obtained from the LAT Data Server[1] where we did a selection of data based on:

- Energy range: 100 MeV – 10 GeV
- Radius: 5° around RA,DEC=(187.8,-14.2)
- Time of interest: January 2017 (MET 504921604–507600005)
- Local zenith of photons: $< 100°$

The cut on the zenith angle of the incoming photons is required due to the contamination caused by the Earth's limb inside the field of view of the telescope. As shown in Figure 5.1 there is a large numbers of photons (in red) coming from close to the limb location (the peak of the gamma emission from the atmosphere is at a zenith angle of 112° [4]), and while all other photons come with a constant rate, these appear as two bright flashes at specific times when the LAT rocks towards the Earth.
In Figure 5.2 the skymap of the detected photons is reported, again the photons related to the effect of the Earth's limb are represented in red. As we can see there is a concentration of photons that denote the presence of the pulsar while the limb contribution is uniform.

[1] `https://fermi.gsfc.nasa.gov/ssc/data/access/lat`

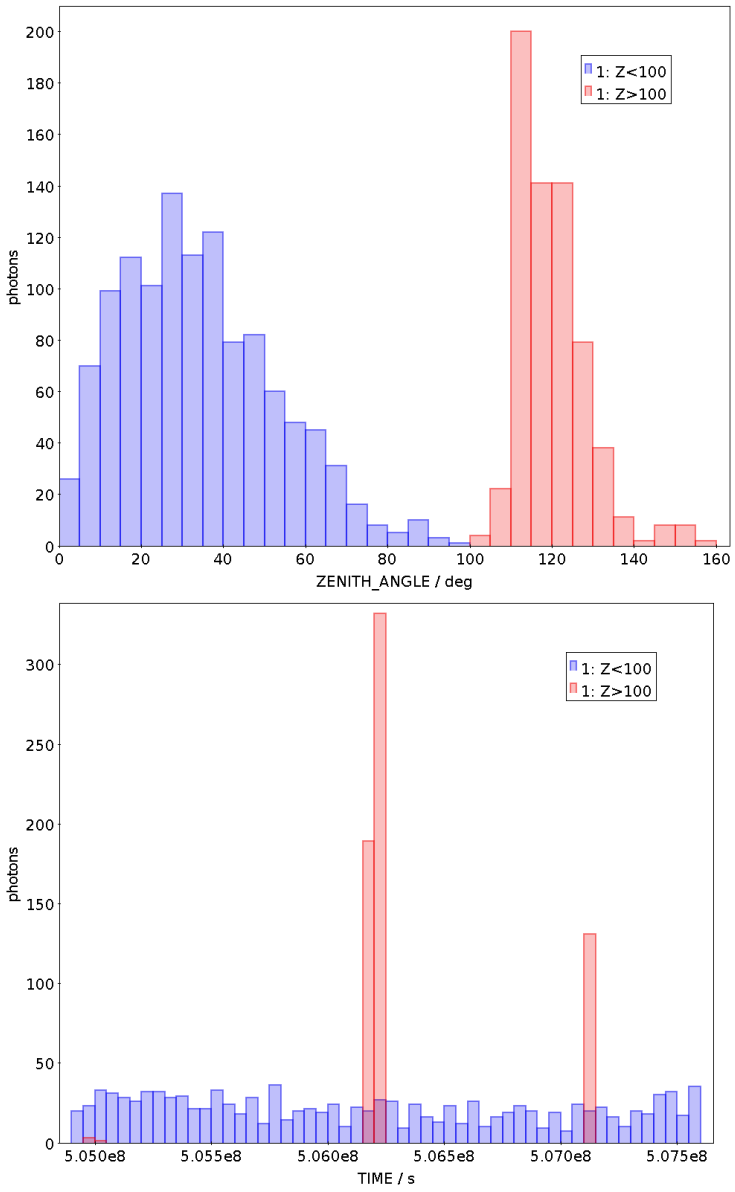

Figure 5.1: Zenith angle cut. Left: distribution of zenith angle for all photons; right: corresponding arrival times.Red: zenith$<$ 100°; red: zenith$>$ 100°.

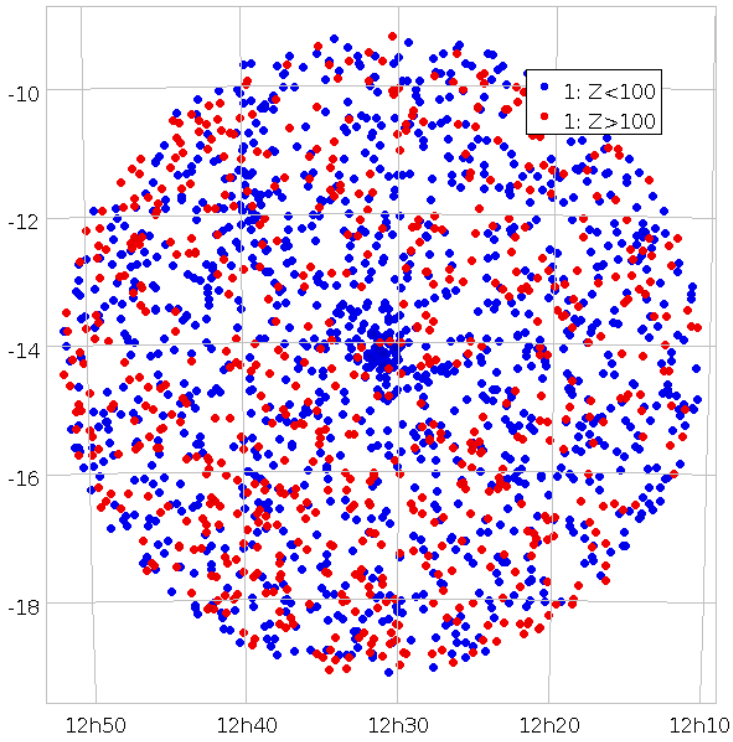

Figure 5.2: Skymap (r.a. and dec.) of the selected data. Color: zenith angle selection.

5.2 `ft2` file

The `ft2` file describes the spacecraft's position during the specified time selection and comes from the *Fermi* database.
For our analysis we tested three files. The reference one is the one we downloaded, with the positions from the NAV filter. The product of this work is the one where we replaced the location of the satellite with those produced by our filter. In addition we prepared another one using the raw GPS positions, cleaned of the outliers with the techniques described above.

5.3 `parfile`

The `parfile` is the ephemeris file for J1231-1411, provided by the *Fermi* LAT collaboration.

5.4 Results

As described in Section 5.2, we compared the result of the timing process of J1231-1411 done with position given by our filter, NAV filter and cleaned GPS data.

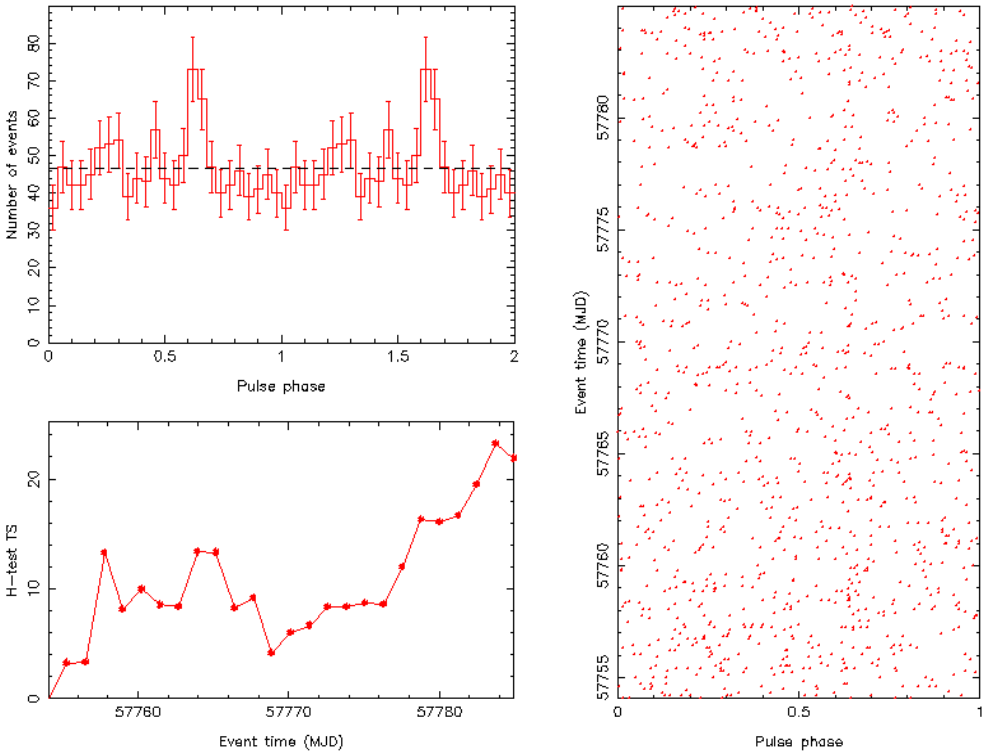

Figure 5.3: Graphical output of a TEMPO2 run with the reference data. Right: scatter plot of photon phase versus time; top left: phase histogram; bottom left: significance of pulse detection versus time.

In Figure 5.3 is reported the graphical output from a TEMPO2 run based on the LAT reference data. At the right of the Figure there is the scatter plot of the

photons' phase as a function of the time of detection. On the left we have the phase histogram (above) and the significance plot (below). The peak emission is observed at a phase between 0.6 and 0.7.

In Figure 5.4 we draw the phase histogram resulting from the timing with the three different position sets. As we can see the differences between the different kind of data are negligible, only one photon presents a little variation.

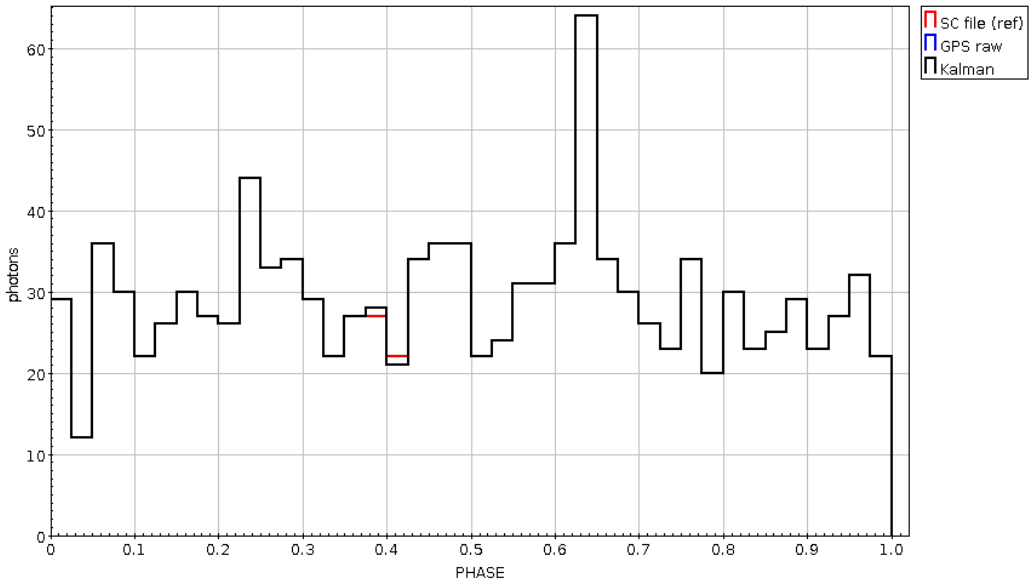

Figure 5.4: Phase histogram for the selected month, obtained with the reference data, with cleaned GPS localization and with this work. The difference is negligible.

Chapter 6

Conclusion

After the validation phase we conclude that the navigation filter, developed with this thesis, works as requested. It is mostly required to smooth outliers in the GPS data, so hopefully it will be a decisive factor only rarely during a mission, when such outliers arise.

The timing process of pulsar J1231-1411 with the data corrected by our filter did not highlight considerable differences with respect to the *Fermi* NAV filter taken as reference.

Remarkably, if we apply our cleaning technique to the GPS data and take the resulting locations we obtain results that are comparable with the others. Therefore, for *a posteriori* position analysis based on the telemetry data it will be sufficient to implement a cleaning code that excludes outliers. The latter appear to be only artefacts related to telemetry packaging in our time interval of 1 month, but we did not investigate the remaining time history looking e.g. for losses of GPS lock. The timing evaluation process allowed us to conclude that even for the analysis of a millisecond pulsar the positional level of accuracy provided by the GPS measurement under nominal operational conditions is enough.

Under nominal conditions, assuming to work on board directly accessing the GPS receiver and spacecraft clock, the most frequent event that will need to be filtered is the loss of GPS lock due to a DOP. Also some unexpected events could happen, like the anomaly of the GPS timing in January 2016 [1]. In these cases the filter will play a crucial role to maintain the satellite positioning accuracy in order to fulfill the scientific requirements.

6.1 Future work

Future improvement of this navigation filter will be focused on its possible use on board of the proposed CubeSat demonstrator for MeV gamma-ray astrophysics by the University of Padova, described in Section 1.3 .

The main feature that needs to be implemented in our filter is the ability to maintain the spacecraft location also in case of loss of GPS lock for long time intervals (several minutes) without drifting respect to the real position. In order to get this feature the dynamic model tested with this filter will need to be upgraded.

The last step will be the implementation of the filter on a CubeSat CPU and a test it directly with a GPS receiver.

Appendix

Software used in this thesis

The implementation of the filter was done with the software MATLAB. The *Fermi* science tools were used for the data selection.

TEMPO2 (see Section 2.5) was used for the pulsar timing process and the software TOPCAT (Tool for OPerations on Catalogues And Tables) was used for the visualization of the `.fits` files.

Fermi GPS receiver data sheet

In the next pages is reported the *Fermi* GPS receiver data sheet, in detail it is a General Dynamics Viceroy-4 GPS receiver.

GENERAL DYNAMICS
Mission Systems

Viceroy®-4 GPS Spaceborne Receiver

Superior positioning with 200+ years of on-orbit performance

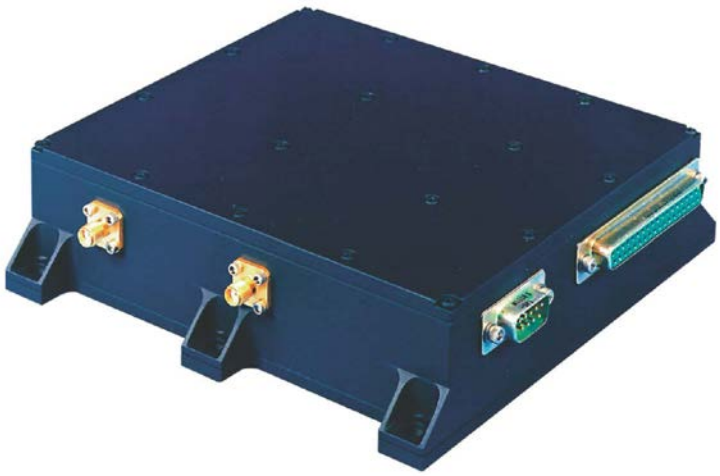

Design based on legacy space qualified digital design

20 years of trouble-free spaceflight heritage

Same reliable position, velocity, time, pseudorange and carrier phase at 1Hz

Same form-factor and interface control as heritage Viceroy receiver

Overview

General Dynamics' Viceroy-4 Global Positioning System (GPS) Spaceborne Receiver provides position, velocity, and time information for Low Earth Orbit (LEO) and Geostationary Earth Orbit (GEO) applications. The use of dual antennas for LEO enhances the performance and satellite visibility. Each of the 12 GPS channels can be assigned to either antenna. The design supports an RS-422 interface.

Key Features

- Space Qualified Digital Design
- Full Spaceborne Capability
- Autonomous Operation
- Pseudorange and Integrated Carrier Phase at One Second Rate
- One PPS Clock Output Synchronized to GPS Time
- Radiation Hardened Static RAM
- Up to 12 Receive Tracking Channels
- 53 Cubic Inches
- 2.4 Pounds
- 20 to 35 VDC Operation
- Improved Radiation Hardened Digital Electronics
- 12 Channels Support All-in-View Tracking
- Dual Antenna – Any Channel Assigned to Either Antenna (LEO only)
- Fast Cold Start Mode Simplifies Integration and Autonomous Operation
- Low Signal Acquisition and Tracking Supports GEO Sidelobe Tracking
- Enhanced Resolution 1 Pulse per Second Output

Standard positioning service in space

Performance Characteristics

Receiver Architecture

- 12 channels with enhanced fast acquisition processor
- Dual antenna – any channel to either antenna (LEO only)
- L1: 1575.42 MHz, C/A code
- Carrier-aided code tracking
- Based on legacy Viceroy architecture (hardware and software)
- Kalman filter or least squares solution

Input/Output

- RS-422 serial I/O (standard)
- X.25 protocol with ECEF position, velocity, time, longitude, latitude, pseudorange, carrier phase
- One pulse per second (GPS, UTC, or Measurement Epoch Time)
- 9-pin male Mirco-D for prime power
- 37-pin female Sub-D for command and telemetry
- SMA female connector for RF signal

Solution Accuracy

- Autonomous Position: < 15 meters, 1 sigma (LEO)
  < 100 meters, 1sigma (GEO)
- Autonomous Velocity: < 0.1 meters/second, 1 sigma (LEO)
  < 0.01 meters/second, 1 sigma (GEO)
- 1PPS time: < 100 ns, 1 sigma (typical)

Time to First Fix

- LEO: 4 minutes, cold start
- GEO: 10 minutes, cold start

Orbital Dynamics

- Altitude: approx 200km to 2000km (LEO)
  approx 35,800km (GEO)
- Velocity: up to 16,000 meters/second
- Acceleration: 1G

Optional and Custom Features: Contact Factory

- Single string or redundant configurations
- Precision internal reference Ovenized Crystal Oscillator (OCXO)
- External 10 MHz reference oscillator
- Time Strobe Input: < 100 ns, 1 sigma
- MEO and HEO Altitudes

Physical/Environmental

- Size: 6.0" x 5.2" x 1.7" (152 x 132 x 43 mm)
- Weight: 2.4 lbs (1.1 kg) max
- DC Power: 8 W max; steady-state tracking (20-35 V)
- Vibration: 17 Grms
- Shock: 1750 G @ 500 Hz
- Temperature: -20°C to +60°C

GENERAL DYNAMICS
Mission Systems

Space Inquiries • 1-877-449-0600 • www.gdmissionsystems.com/space • www.gdmissionsystems.com/contact-us

D-VICEROY4-02-0919
PRI-1908-0054

Bibliography

[1] https://www.navcen.uscg.gov/pdf/gps/AirForceOfficialPressRelease.pdf.

[2] A. A. Abdo. Fermi large area telescope observations of the crab pulsar and nebula. *The Astrophysical Journal*, 708(2):1254–1267, dec 2009.

[3] A. A. Abdo, M. Ajello, A. Allafort, L. Baldini, J. Ballet, G. Barbiellini, M. G. Baring, D. Bastieri, A. Belfiore, R. Bellazzini, and et al. The second fermi large area telescope catalog of gamma-ray pulsars. *The Astrophysical Journal Supplement Series*, 208(2):17, Sep 2013.

[4] M. Ackermann et al. Inferred Cosmic-Ray Spectrum from Fermi Large Area Telescope γ-Ray Observations of Earth's Limb. *Phys. Rev. Lett.*, 112:151103, 2014.

[5] S. Andreetta. Study of material activation in nanosatellites for gamma-ray astrophysics. http://tesi.cab.unipd.it/56942, 2017.

[6] W. B. Atwood. The large area telescope on the fermi gamma-ray space telescope mission. *The Astrophysical Journal*, 697(2):1071–1102, may 2009.

[7] F. Berlato. Design and optimization around 1 mev of a calorimeter for a cubesat mission. http://tesi.cab.unipd.it/53502, 2016.

[8] P.F Bloser, R Andritschke, G Kanbach, V Schönfelder, F Schopper, and A Zoglauer. The mega advanced compton telescope project. *New Astronomy Reviews*, 46(8-10):611–616, Jul 2002.

[9] S. Canevarolo. Sensitivity of a compton nanosatellite for gamma-ray burst observations. http://tesi.cab.unipd.it/61390, 2018.

[10] P. A. Caraveo. Gamma-ray pulsar revolution. *Annual Review of Astronomy and Astrophysics*, 52(1):211–250, Aug 2014.

[11] A. De Angelis, V. Tatischeff, I.A. Grenier, J. McEnery, M. Mallamaci, M. Tavani, U. Oberlack, L. Hanlon, R. Walter, A. Argan, and et al. Science with e-astrogam. *Journal of High Energy Astrophysics*, 19:1–106, Aug 2018.

[12] R. T. Edwards, G. B. Hobbs, and R. N. Manchester. Tempo2, a new pulsar timing package - ii. the timing model and precision estimates. *Monthly Notices of the Royal Astronomical Society*, 372(4):1549–1574, Nov 2006.

[13] fermi.gsfc.nasa.gov. `https://fermi.gsfc.nasa.gov/ssc/data/access/lat/ephems/index.html`.

[14] L. Guillemot. `https://fermi.gsfc.nasa.gov/ssc/data/analysis/user/Fermi_plug_doc.pdf`.

[15] M. E. Hough. Precise orbit determination using satellite radar ranging. *Journal of Guidance, Control, and Dynamics*, 35(4):1048–1058, 2012.

[16] M. Karaim, M. Elsheikh, and A. Noureldin. Gnss error sources. In Rustam B. Rustamov and Arif M. Hashimov, editors, *Multifunctional Operation and Application of GPS*, chapter 4. IntechOpen, Rijeka, 2018.

[17] M. Kerr. Improving sensitivity to weak pulsations with photon probability weighting. *The Astrophysical Journal*, 732(1):38, apr 2011.

[18] E. Kim, S. Han, and A. M. A. Sayegh. Sensitivity of the gravity model and orbital frame for on-board real-time orbit determination: Operational results of gps-12 gps receiver. *Remote Sensing*, 11(13):1542, Jun 2019.

[19] D. R. Lorimer and M. Kramer. *Handbook of Pulsar Astronomy*, volume 4. 2004.

[20] G. Lucchetta, F., R. Rando, D. Bastieri, and G. Urso. Scientific performance of a nano-satellite MeV telescope. *The Astronomical Journal*, 153(5):237, apr 2017.

[21] J. Mcenery, J. A. Barrio, I. Agudo, M. Ajello, J.-M. Álvarez, S. Ansoldi, S. Anton, N. Auricchio, J. B. Stephen, L. Baldini, et al. All-sky medium energy gamma-ray observatory: Exploring the extreme multimessenger universe. *arXiv preprint arXiv:1907.07558*, 2019.

[22] R. Dal Moro. Evaluating the flux of cosmic protons along the orbit of a compton gamma-ray space telescope. `http://tesi.cab.unipd.it/60812`, 2018.

[23] R. Rando, S. Canevarolo, H. Xiao, and D. Bastieri. Sensitivity to gamma-ray bursts of a nanosatellite MeV telescope with a silicon tracker. *The Astronomical Journal*, 158(1):42, jul 2019.

[24] D. Rose. International space station familiarization. technical report td 9702, nasa (1998).

[25] G. Seeber. *Satellite Geodesy*. Walter de Gruyter, 2003.

[26] H. Toyoizumi, M. Genda, K. Yui, T. Yamada, and Y. Hieda. Improvement of the accuracy of pps signal. 2005:1713–1719, 01 2005.

[27] D.A. Vallado and W.D. McClain. *Fundamentals of Astrodynamics and Applications*. Fundamentals of Astrodynamics and Applications. Microcosm Press, 2001.